

# Ionic Transport in Potential Coating Materials for Mg Batteries

Tina Chen,<sup>†,‡</sup> Gopalakrishnan Sai Gautam,<sup>\*,¶</sup> and Pieremanuele Canepa<sup>\*,§</sup>

<sup>†</sup>Department of Materials Science and Engineering, University of California, Berkeley, Berkeley, California 94720, United States

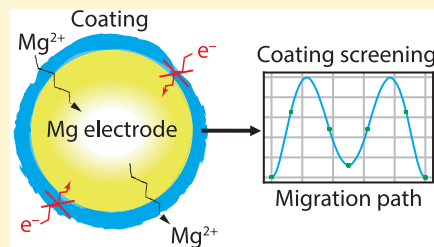
<sup>‡</sup>Materials Science Division, Lawrence Berkeley National Laboratory, Berkeley, California 94720, United States

<sup>¶</sup>Department of Mechanical and Aerospace Engineering, Princeton University, Princeton, New Jersey 08544, United States

<sup>§</sup>Department of Materials Science and Engineering, The National University of Singapore, 117576, Singapore

## Supporting Information

**ABSTRACT:** A major bottleneck for the development of Mg batteries is the identification of liquid electrolytes that are simultaneously compatible with the Mg-metal anode and high-voltage cathodes. One strategy to widen the stability windows of current nonaqueous electrolytes is to introduce protective coating materials at the electrodes, where coating materials are required to exhibit swift Mg transport. In this work, we use a combination of first-principles calculations and ion-transport theory to evaluate the migration barriers for nearly 27 Mg-containing binary, ternary, and quaternary compounds spanning a wide chemical space. Combining mobility, electronic band gaps, and stability requirements, we identify  $\text{MgSiN}_2$ ,  $\text{MgI}_2$ ,  $\text{MgBr}_2$ ,  $\text{MgSe}$ , and  $\text{MgS}$  as potential coating materials against the highly reductive Mg metal anode, and we find  $\text{MgAl}_2\text{O}_4$  and  $\text{Mg}(\text{PO}_3)_2$  to be promising materials against high-voltage oxide cathodes (up to  $\sim 3$  V).



## 1. INTRODUCTION

Mg batteries operating with a Mg-metal anode set a practical alternative to state-of-the-art Li-ion batteries by providing increased volumetric capacities ( $\sim 3833 \text{ mAh}/\text{cm}^3$  for Mg versus  $\sim 800 \text{ mAh}/\text{cm}^3$  for Li insertion into graphite) at a lower cost.<sup>1–3</sup> The primary advantage of Mg batteries is the use of the metallic anode since Mg can be safely plated and stripped, dendrite-free, from electrolytic solutions at acceptable current densities ( $\sim 0.5\text{--}1.0 \text{ mA}/\text{cm}^2$ ).<sup>2</sup> While the possibility of plating dendrite-free Mg has been recently challenged by Davidson et al.<sup>4</sup> and Ding et al.,<sup>5</sup> the shape of the electrodes employed in the former and the inappropriate classification of globular Mg deposits as dendrites in the latter cast doubt on the formation of Mg dendrites under practical battery conditions.<sup>6</sup> While Davidson et al. observe that sharp edges and/or a rough surface at the Mg electrode can lead to the nucleation and growth of dendrites,<sup>4</sup> the potential usage of a metallic, dendrite-free, and safe anode still remains one of the main advantages of Mg-based electrochemical storage.

Nevertheless, a functioning Mg battery is challenged by the poor chemical and electrochemical stability of a handful of liquid electrolytes,<sup>2,7</sup> which are compatible with either the Mg-metal anode or a high-voltage cathode, but not with both electrodes simultaneously. The decomposition of liquid electrolytes on electrodes can lead to the formation of passivating layers that permanently block the electrochemical function of a battery. For example, the formation of a passivating  $\text{MgO}$  layer on the Mg-metal surface<sup>1,3</sup> or at the high-voltage cathode<sup>8,9</sup> has led to rapidly diminishing electrochemical capacities with cycling. Furthermore, such unstable electrolytes can lead to safety issues due to the presence of

flammable solvents, as has been observed in Li-ion electrolytes.<sup>10,11</sup>

One strategy to mitigate the safety challenges of liquid electrolytes is using a less flammable solid material (i.e., a solid electrolyte) capable of transporting Mg ions efficiently. While two examples of such materials exist in the multivalent chemical space, namely,  $\text{MgSc}_2\text{X}_4$  ( $\text{X} = \text{S}, \text{Se}$ )<sup>12</sup> and  $\text{ZnPS}_3$ ,<sup>13</sup> using chalcogenide chemistries to boost multivalent mobility typically correlates with poor electrochemical stabilities and increased electronic conductivity.<sup>12,14,15</sup> Note that electronic conductivity within a solid electrolyte is a source of self-discharge and is detrimental to battery performance.

A practical way to solve the inherent liquid/solid electrolyte instability is to develop protective coating materials that can selectively mitigate detrimental decomposition reactions against highly oxidizing cathodes and/or the highly reducing Mg metal. In practice, the identification of protective coatings consists of identifying a number of materials whose electrochemical stability window (ESW)<sup>16,17</sup> is sufficiently large that it spans across the HOMO (or LUMO) level of a liquid electrolyte and the chemical potential of the cathode (or anode). Subsequently, candidate coating materials can either be deposited as thin ( $\sim$ nanoscale) layers via *ex situ* methods or can be formed *in situ* via the reaction of a strategically chosen electrolyte (and additives in liquid electrolytes) and the electrodes.<sup>18–22</sup>

One potential difference between *ex situ* and *in situ* methods of forming coating materials is the resulting electronic

Received: July 7, 2019

Revised: September 5, 2019

Published: September 6, 2019

conductivity. In general, a higher electronic conductivity in a coating than the electrolyte is detrimental to the stability of the electrolyte. This is because the drop/gain in chemical potential across the coating may not be sufficient enough to protect the electrolyte from reduction/oxidation.<sup>23</sup> Additionally, a thicker coating layer accommodates a higher chemical potential difference and becomes more suitable for accommodating an electrolyte with a small ESW. Hence, the choice and thickness of a coating (and its electronic conductivity) can be calibrated depending on the intrinsic electronic conductivity of the electrolyte in *ex situ* methods. However, if a coating is obtained via *in situ* reactions at the electrode||electrolyte interface, a careful analysis of the properties (ESW and electronic conductivity) of the phase formed at the interface will be necessary to ensure that the battery does not exhibit self-discharge. Nevertheless, a candidate coating is optimal if it exhibits a sufficiently large ESW and a significantly low electronic conductivity.

Recently,<sup>24</sup> we reported the ESWs of several Mg-containing compounds, which can be potential coating materials for Mg batteries. The set of Mg-containing compounds investigated includes various Mg-binaries and Mg-ternaries, as well as some compounds containing a non-Mg metal, such as Sc, Ti, Nb, Zr, Al, Ga, and In because they are either commonly used as coating materials in Li-ion batteries or have been considered as Mg ionic compounds in previous studies. We estimated the ESWs via the construction of grand-potential phase diagrams based on density functional theory (DFT) calculations.<sup>25</sup> From the calculated ESWs, we identified binary Mg-halides ( $MgF_2$ ,  $MgCl_2$ ,  $MgBr_2$ , and  $MgI_2$ ) and  $Mg(BH_4)_2$  as possible anode coating candidates and  $MgF_2$ ,  $Mg(PO_3)_2$ , and  $MgP_4O_{11}$  as potential cathode coatings. Analogous work by Snydacker et al.<sup>26</sup> also proposed a subset of the aforementioned materials. However, the utilization of these proposed materials as effective coatings demands that  $Mg^{2+}$  transport in their structures is facile under battery operating conditions. Hence, it is paramount to evaluate the Mg mobility on any candidate coating.

Using first-principles calculations, we systematically assess the barriers and band gaps for Mg migration in a total of 27 candidate coating materials. This set of candidate materials was obtained based on the screening done for identifying coatings with promising electrochemical stability in ref 24, which resulted in the chemistries listed above. Additionally, we included a set of materials that have been predicted to be stable against Mg metal,<sup>24,26</sup> such as  $MgSiN_2$ ,  $MgH_2$ ,  $MgB_2$ ,  $Mg_2Ge$ ,  $Mg_2Si$ ,  $Mg_3As_2$ ,  $Mg_3P_2$ ,  $Mg_3N_2$ ,  $MgTe$ ,  $MgSe$ ,  $MgS$ , and  $MgO$ , and materials with promising oxidative stability (>3 V), such as  $Mg_{0.5}Ti_2(PO_4)_3$ ,  $MgAl_2O_4$ ,  $MgB_4O_7$ , and  $MgS_2O_7$ . Further, we considered several Mg analogues (e.g.,  $Mg(NbO_3)_2$ ) of promising Li coating materials (e.g., Li–Nb oxides),<sup>18–22</sup> and Mg binaries ( $MgB_4$ ,  $MgB_7$ , and  $MgP_4$ ) that may be kinetically stable against Mg-metal, resulting in a total of 27 candidates. Although prior studies have demonstrated<sup>27–30</sup> that the lack of Mg (or multivalent) mobility in several structures relates to a combination of stronger electrostatic interactions of a 2+ charge with its surrounding anion environment (versus 1+ charge of monovalent ions) and strong coordination preferences,<sup>17,25,31–34</sup> Mg mobility has not been rigorously quantified yet for potential coating chemistries.

Since the range of thickness in coating materials is often limited to a few tens of nanometres (0.5–50 nm),<sup>35</sup> the stringent criteria for ionic mobility required in cathodes or

(solid) electrolytes can be slightly relaxed in coating materials. Thus, we used a range of maximum Mg migration barriers, namely, ~600–980 meV, to identify candidates that can operate under a variety of battery conditions (see Section 2). Based on these limits and the calculated migration barriers, we have identified  $MgSiN_2$ ,  $MgI_2$ ,  $MgBr_2$ ,  $MgSe$ , and  $MgS$  as potential anode coatings and  $MgAl_2O_4$  and  $Mg(PO_3)_2$  as potential cathode coatings. We also analyzed the migration topology and the energy required to form Mg diffusion carriers in a set of candidate coatings and found significant similarities to topologies observed in ternary Mg oxides. Finally, our work will offer useful guidance in understanding the electrochemical stability, Mg mobility, and electronic properties in several Mg-containing compounds and enable the development of practical Mg batteries.

## 2. MIGRATION BARRIER THRESHOLDS IN COATING MATERIALS FOR MG BATTERIES

The assessment of microscopic migration barriers to evaluate the ability of macroscopic Mg transport in coating materials becomes relevant only if the calculated barriers can be connected to macroscopic properties, such as diffusion coefficients,  $D$ . Using the Arrhenius expression of eq 1, we can estimate the diffusivity of a given ion (e.g.,  $Mg^{2+}$ ) in a solid, given a barrier along a microscopic (or local) migration pathway ( $E_m$ ).

$$D = fa^2 \nu \exp\left(-\frac{E_m}{k_B T}\right) \quad (1)$$

where  $a$ ,  $\nu$ ,  $f$ ,  $k_B$ , and  $T$  are the hopping distance along a migration pathway, vibrational frequency of Mg in a host structure, correlation factor, Boltzmann constant, and temperature, respectively. Typically,  $a$  and  $\nu$  are of the order of ~3 Å and  $10^{12}$  Hz, respectively, and do not vary significantly in most solids.<sup>36</sup> Thus, the governing variable for  $D$  in eq 1 is  $E_m$ , which is a chemistry (oxides vs sulfides), structure (layered vs spinel), and pathway (tetrahedral → octahedral → tetrahedral or octahedral → tetrahedral → octahedral) dependent property. Additionally, we only consider local migration pathways that form percolating networks,<sup>36,37</sup> i.e., pathways that are sufficiently connected through the lattice, enabling Mg to diffuse from one end of the lattice to the other along at least one crystallographic direction.

We assume that ionic diffusion follows a random-walk behavior without any long-range correlation effects between Mg sites, i.e.,  $f \sim 1$  in eq 1. Further, the diffusion length  $l$  of  $Mg^{2+}$  across a coating layer (of thickness ~ $l$ ) scales as

$$l = \sqrt{Dt} \quad (2)$$

with  $t$  the time for (dis)charge, i.e., the time taken for  $Mg^{2+}$  to diffuse through the coating layer. By fixing the time  $t$  to (dis)charge a battery, at a given thickness of coating layer (i.e., the diffusion length), one arrives at a minimum required Mg-diffusivity,  $D_{min}$  via eq 2, which is equivalent to a maximum tolerable migration barrier ( $E_m^{max}$ ) from eq 1. Thus, potential candidates are those that exhibit values of  $E_m$  lower than  $E_m^{max}$ .

Figure 1 illustrates mobility considerations, which sets general guidelines, apart from thermodynamic stability, for material selection in batteries (including Li- and Na-systems), which we apply to identify potential Mg coatings. Figure 1 plots  $E_m^{max}$  at various thicknesses (or equivalently particle sizes), which sets  $l$ , and (dis)charge rates of potential coating

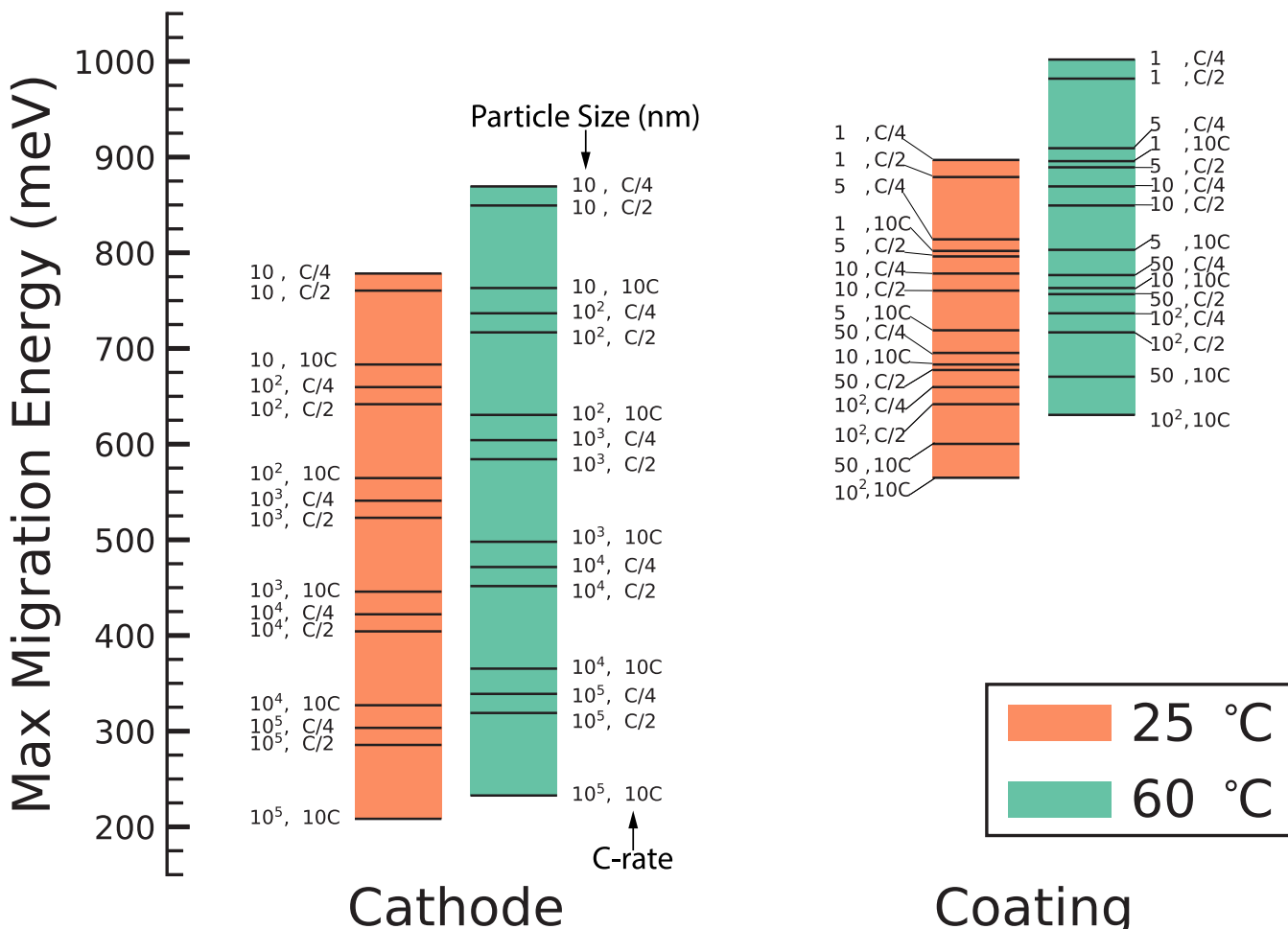


**Figure 1.** Maximum tolerable migration barriers ( $E_m^{\max}$ ) in cathode and coating materials for different sizes of cathode particles and different thicknesses of coating layers, operating at different (dis)charge rates (in units of C-rate) and at two different temperatures (25 and 60 °C). The particle sizes/layer thicknesses are given in units of nanometers.

materials (or cathode)<sup>3,31</sup> that determine  $t$ . While changes in temperature affect the value of  $D_{\min}$  (and  $E_m^{\max}$ ), typical Mg batteries are cycled at 60 °C to mitigate the poor kinetics of Mg<sup>2+</sup> diffusion.<sup>1,38</sup> Hence, we include both room temperature (orange bar, Figure 1) and 60 °C (green bar) to estimate  $E_m^{\max}$ .

In Figure 1, we consider rates of (dis)charge for battery operations ranging from extremely fast (dis)charging at 10C (i.e., 6 min) to C/4 (4 h). Typically, slow (dis)charge regimes are closer to the conditions of thermodynamic equilibrium and are used for laboratory-scale experiments, while fast charging<sup>39</sup> has become more prevalent in portable electronics recently. Consequently, the combination of low (dis)charge rates and high temperatures allows the operation of coating materials (and cathodes) with higher migration barriers. For example, a coating layer of thickness ~50 nm operating at 25 °C and 10C can tolerate  $E_m^{\max}$  of ~600 meV, while a similarly thick coating layer at 60 °C and C/4 can accommodate  $E_m^{\max} \sim 777$  meV.

Cathode particles in Li-ion batteries are routinely coated with layers ranging in thickness between 1 and 50 nm.<sup>19,40</sup> Thus, the thickness of coating layers is normally 1–2 orders of magnitude lower than that of cathode particles,<sup>18–22,35</sup> which is reflected in a higher tolerable  $E_m^{\max}$  for coatings compared to cathodes (Figure 1). Coating layer thickness can also vary depending on the synthesis and processing techniques utilized. For example, atomic layer deposition (ALD) can produce

coatings thinner than a nanometer while pulsed laser deposition (PLD) typically yields thicker coatings (50–1000 nm).<sup>35</sup> Hence, given a variety of operating conditions that require different  $E_m^{\max}$  for coatings (Figure 1), we select two specific cases to represent “reasonable”, yet significantly different, battery operating conditions: (i) 50 nm coating thickness at 25 °C and 10C which yields  $E_m^{\max}$  of ~600 meV and (ii) 1 nm coating thickness at 60 °C and C/2 resulting in  $E_m^{\max}$  of ~980 meV. Nevertheless, a thermodynamically stable coating material with a low migration barrier (<400 meV) will always be ideal.

### 3. METHODS

**3.1. First-Principles Calculations.** To calculate the  $E_m$  for a migration pathway in a given structure of a candidate coating material, we employ the nudged elastic band (NEB) method<sup>41,42</sup> coupled with density functional theory (DFT) calculations,<sup>43,44</sup> as implemented in the Vienna ab initio simulation package (VASP).<sup>45,46</sup> The exchange and correlation energy are approximated with the Perdew–Burke–Ernzerhof (PBE)<sup>47</sup> functional. The total energy is sampled on a well-converged  $k$ -point mesh with a grid density of 1000/atom together with the projector-augmented wave (PAW) theory<sup>48</sup> and a 520 eV plane-wave cutoff for the valence electrons. Unless otherwise mentioned, for each compound considered, we evaluate  $E_m$  in its ground state configuration as per the Materials Project (MP) database.<sup>49</sup> Supercells used for NEB calculations introduce a minimum distance of at least 8 Å between the migrating Mg ions

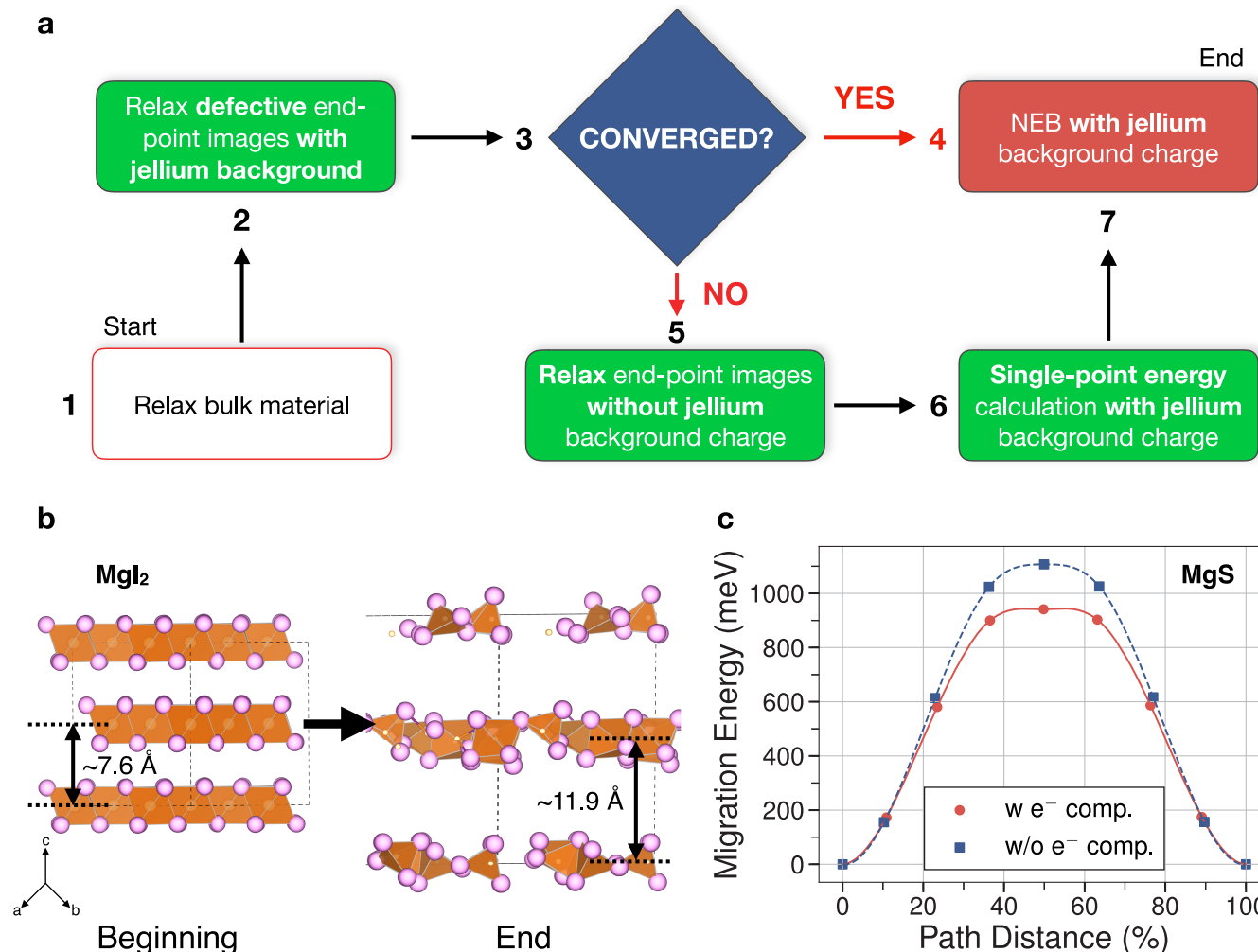


**Figure 2.** (a) Flowchart to accurately compute migration barriers in charge-compensated candidate coating systems. (b) Example of failed convergence of end-point images in MgI<sub>2</sub> in the presence of a jellium background resulting in significant distortion of layers of edge-sharing MgI<sub>6</sub>. The structural distortion is highlighted by the change in interlayer distance before ( $\sim 7.6 \text{ \AA}$ ) and after relaxation ( $\sim 11.9 \text{ \AA}$ ). (c) Comparison of migration energies for Mg ions in MgS after the structure relaxation of the end-point images with jellium background charge (red dots) and without jellium (blue squares). Numbers near each box guide the execution of the flowchart described in the text.

to minimize fictitious interactions across periodic boundaries. The total energy is converged within  $10^{-5} \text{ eV}$  per supercell. The end-point structures, i.e., the initial and final states along the Mg migration pathway, are fully relaxed until the forces on the atoms converged within  $10^{-2} \text{ eV/\AA}$ , whereas the NEB forces are converged within  $0.05 \text{ eV/\AA}$ . Unless noted differently, seven distinct images are used between the end points to evaluate the ion migration trajectory. For calculating formation energies of Mg vacancies (see Section 3.4), we use the PBE functional and create supercells from PBE-relaxed geometries. Subsequently, we relax only the ionic positions after a Mg vacancy has been introduced within the supercell to calculate the total energy of a defective structure.

Band-gaps of the materials studied are evaluated from the density of states (DOS) computed with the hybrid (25% Hartree–Fock) range-separated exchange-correlation functional, HSE06.<sup>50–52</sup> For DOS calculations, we fully relaxed the coordinates, cell, and shape of the bulk unit cells, in accordance with the input settings used in the MP.<sup>53</sup> Notably, the band gap predictions with HSE06 show good agreement with experiments and/or other theoretical calculations. For example, our HSE06 calculated band gaps for Mg<sub>2</sub>Si ( $\sim 0.83 \text{ eV}$ ) and Mg<sub>2</sub>Ge ( $\sim 0.61 \text{ eV}$ ) are similar to previous studies, namely,  $\sim 0.77\text{--}0.8 \text{ eV}$  for Mg<sub>2</sub>Si and  $\sim 0.67\text{--}0.74 \text{ eV}$  for Mg<sub>2</sub>Ge.<sup>54</sup> In the case of Mg vacancy formation calculations (Section 3.4), we use DOS calculated using the PBE functional to evaluate band gaps in order to be

consistent with the level of theory used to calculate the total energies of the defective and defect-free structures.

### 3.2. Challenges in Computing Migration Barriers in Coating Materials.

The DFT+NEB framework has been employed to evaluate  $E_m$  for a wide variety of electrode structures<sup>3,55</sup> containing open-shell transition metals, owing to lower computational costs compared to *ab initio* molecular dynamics (AIMD) simulations, and hence represents the standard to evaluate ionic migration barriers in solids. However, a number of challenges remain when the DFT+NEB methodology is applied to materials containing closed-shell nonredox-active (transition) metals, as in the case of coating materials.

Typically, migration barriers are evaluated in two limits of Mg<sup>2+</sup> concentration: (i) low vacancy limit, where the barrier for the migration of an isolated Mg-vacancy is evaluated, and (ii) high vacancy limit, i.e., migration barrier of an isolated Mg<sup>2+</sup>. In both scenarios, Mg ions hop via a site-vacancy (or an interstitial-based) mechanism, where the diffusion carrier (Mg vacancy or interstitial) is introduced and the migration barrier of the carrier is evaluated on all possible paths that can give rise to long-range Mg diffusion. We assess Mg migration in the low-vacancy limit, i.e., one Mg vacancy per supercell, for all the coating materials considered in this work.

To maintain the charge neutrality of the underlying structure upon introducing the Mg vacancy (or Mg atom), the valence electrons of the removed (added) Mg atom must be reintroduced (removed) in

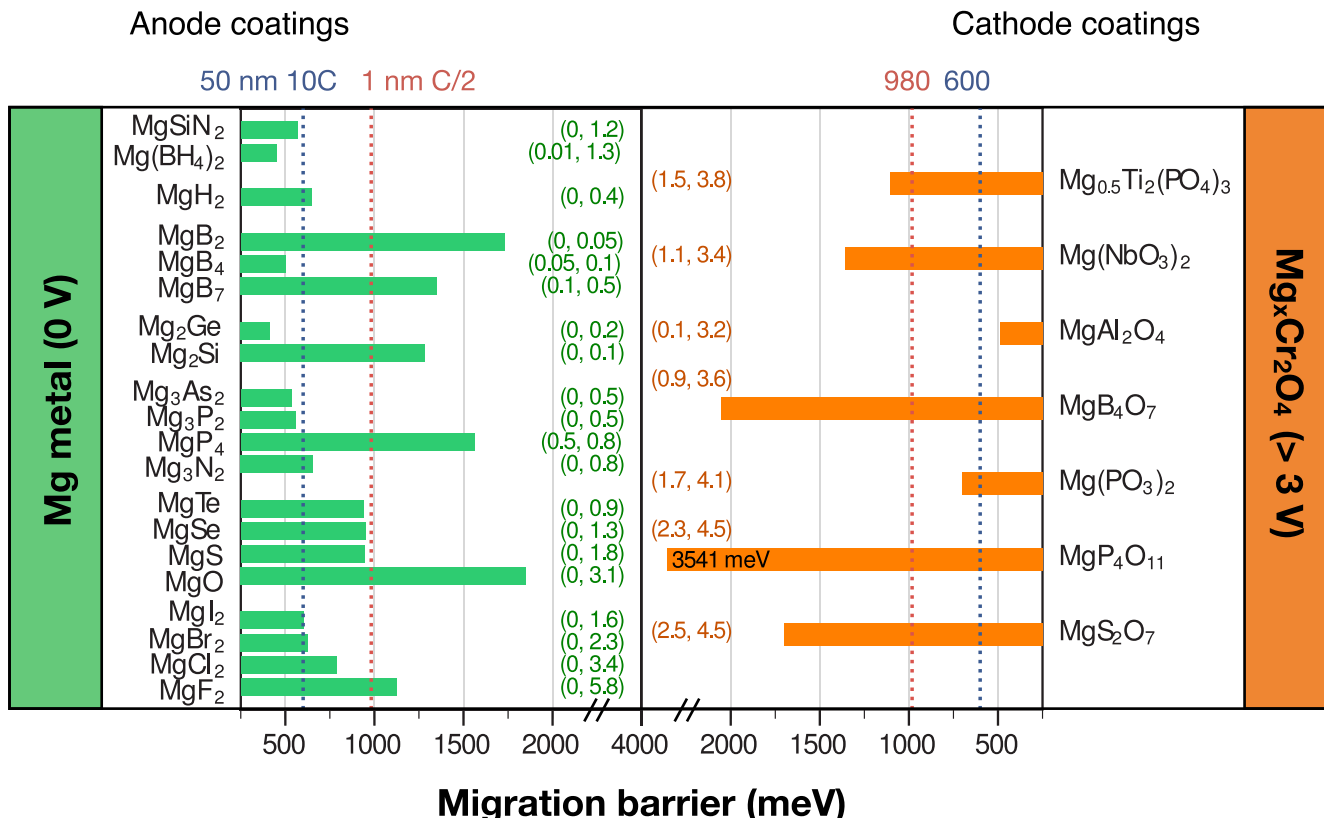


**Figure 3.** Calculated migration barriers for anode (left) and cathode (right) coating candidates. Dotted vertical lines indicate strict (~600 meV, blue) and lenient (~980 meV, red)  $E_m^{\max}$  values (see Section 2). The numbers in brackets provide the (reductive, oxidative) stability limits, in V vs Mg metal, as reported by Chen et al.<sup>24</sup> The  $E_m$  for  $Mg(BH_4)_2$  should exhibit a higher error than other materials due to challenges in converging the NEB.

the simulation cell; i.e., the charge imbalance created by a local Mg diffusion carrier should be compensated by the addition/removal of electrons. For semiconducting/insulating cathode materials that contain open-shell redox-active species (e.g., 3d/4d transition metals), the addition (removal) of electrons is accommodated by a change in the oxidation state of a “nearby” redox-active species. In the case of metallic electrodes, local charge imbalances are efficiently screened by the metal electron density and do not have to be explicitly accounted for in DFT calculations.

However, the addition/removal of electrons with the creation of local Mg carriers is required for candidate coatings in DFT calculations since most of the candidates: (i) are highly stoichiometric and have elements with well-defined oxidation states, (ii) do not contain any redox-active species, and (iii) are nonmetallic. Thus, modeling Mg migration in potential coatings requires “charge compensation”. Since NEB calculations are performed with periodic boundary conditions, the additional electrons for charge compensation are introduced as a homogeneous background charge, termed “jellium”. To minimize the number of additional electrons that contribute to the jellium background compensating one Mg vacancy, we used the soft-core Mg PAW potential with only two valence electrons [ $s^2p^0$ ] in our DFT+NEB calculations. Also, we use supercells with jellium background which provide a migration barrier within a  $\pm 50$  meV accuracy threshold, when compared to calculations performed in larger supercells (see Section S3 of the Supporting Information). Note that, in a practical battery device, local charge imbalances in nonmetallic coatings are usually compensated either by Mg-atom transfer at the coating||electrode interface or through intrinsic defects already present in the material.

**3.3. Workflow To Assess Mg Migration Barriers.** While previous reports have used the jellium background for charge compensation and computed migration barriers, the accuracy of this

approach has not been reliably tested.<sup>17,33,56,57</sup> In particular, it is challenging for any self-consistent procedure, such as DFT with a semilocal PBE functional, to appropriately localize the jellium charge, leading to problematic convergence of the charge density, the total energy, and the atomic forces. Poor convergence of the charge density can eventually cause appreciable deformation of the underlying structure, such as significant rearrangement of atomic positions and/or large changes in volume or shape, resulting in an inability to accurately assess migration barriers via the NEB method. In our work, we encountered significant structural distortions owing to poorly converged charge density in the  $MgX_2$  (X = Cl, Br, and I) structures, where layers of edge-sharing  $MgX_6$  octahedra are highly distorted upon structure relaxation in the presence of a jellium background, as depicted for  $MgI_2$  in Figure 2b.

To ensure that our structural model retains charge neutrality while not exhibiting major structural distortions, we adopt the workflow of Figure 2a to compute the migration barriers. This strategy can be implemented whenever the introduction of a compensating background charge leads to unphysical structures.

The workflow of Figure 2a is as follows:

1. Relax (coordinate, shape, and volume) the charge-neutral bulk material with DFT computational settings (see Section 3.1).
2. Relax (coordinate, shape, and volume) the end-point structures, including one or multiple diffusing carriers (Mg vacancies in our case). In this step, the vacancies of the migration species are explicitly charge compensated with the jellium background.
3. Verify convergence of end-point geometries. Specifically, ensure that the relaxed end-point geometries are not significantly different from the starting structure. If the end points are satisfactorily converged, proceed to step 4, else proceed to step 5.

4. Perform a NEB where each interpolated site (or image) along the elastic band is charge-compensated, similar to the end points, and extract the migration barrier.
5. Relax (coordinate, shape, and volume) the end points without charge compensation, ensuring that the relaxed geometries do not exhibit significant distortions, and proceed to step 6. If the relaxed end points are significantly perturbed from the starting geometries, accurate migration barriers can only be assessed using more computationally expensive techniques (e.g., AIMD) and/or by using a better functional to describe the electronic exchange-correlation (e.g., hybrid functionals).
6. Using the relaxed geometries from step 5, perform a single self-consistent field calculation for the end points incorporating charge compensation.
7. Using the relaxed geometries of step 5, construct the elastic band and perform an NEB calculation including charge compensation. The barrier is extracted using the total energies of the end points from step 6.

In systems that do not exhibit significant structural distortion when charge compensation is included in the end-point relaxation calculation, e.g., MgS after step 3, the migration barrier evaluated using step 4 (~941 meV, red line in Figure 2c) is significantly lower (~160 meV) compared to that obtained using steps 5–7 (~1107 meV, blue line in Figure 2c). Hence, we expect the barriers evaluated using steps 5–7 for the  $MgX_2$  ( $X = Cl, Br$ , and I) structures to be over(under)estimated by  $\sim \pm 160$  meV, which is equivalent to approximately 3 orders of magnitude difference in diffusivity (from eq 1). Unless explicitly mentioned, all systems other than  $MgX_2$  ( $X = Cl, Br$ , and I) are investigated using steps 1–4, with an accuracy of  $\pm 50$  meV for the DFT+NEB framework.<sup>31,58</sup>

**3.4. Calculating Mg Vacancy Formation Energies.** The occurrence of a Mg vacancy, with a specific charge  $q$ , that enables Mg migration in a material can be estimated via the formation energy  $E^f[Mg^q]$  by eq 3.

$$E^f[Mg^q] = E_{\text{Tot}}[Mg^q] - E_{\text{Tot}}[\text{bulk}] + \mu_{\text{Mg}} + qE_{\text{Fermi}} + E_{\text{corr}} \quad (3)$$

$E_{\text{Tot}}[Mg^q]$  and  $E_{\text{Tot}}[\text{bulk}]$  are the DFT total energies of a sufficiently large supercell with and without a Mg vacancy, respectively.  $\mu_{\text{Mg}}$  is the chemical potential of Mg, as determined by the set of phases in thermodynamic equilibrium with the coating at 0 K, with the range of relevant  $\mu_{\text{Mg}}$  identified by the ESW of each coating (see details in Section 4.3).  $E_{\text{Fermi}}$  is the Fermi energy of electrons and can range between the valence and conduction band edges of the defect-free coating material.  $E_{\text{corr}}$  is the electrostatic correction term to account for spurious interactions between the charged defect and its periodic images (long-range effects) and interactions of the charged defect with the compensating jellium background (short-range).<sup>15</sup> For charge-compensated Mg vacancies (i.e.,  $q = -2$ ), we evaluated  $E_{\text{corr}}$  using the correction scheme proposed by Freysoldt et al.<sup>59</sup> for isotropic structures and its generalization formulated by Kumagai and Oba<sup>60</sup> for anisotropic structures, with representative plots of the correction schemes in considered defects shown in Supporting Information Section S4. Note that evaluating Mg vacancy formation across the 27 candidates considered in this work carries a significant computational expense. Thus, we restrict to calculating  $E^f[Mg^q]$  in the same set of candidates in which we analyzed the Mg migration topologies, i.e.,  $MgAl_2O_4$ ,  $MgSiN_2$ , and  $MgBr_2$ . We use the Kröger–Vink notation<sup>61</sup> to represent defects, where  $V$  stands for vacancy.

## 4. RESULTS

### 4.1. Mg Migration Barriers in Candidate Materials.

Figure 3 shows the calculated migration barriers for potential binary, ternary, and quaternary coating materials for anodes (left, green bars) and cathodes (right, orange bars), as well as their calculated reductive and oxidative stabilities (numbers in parentheses, in units of V vs Mg metal). The computed migration barriers are compared against  $E_m^{\text{max}}$  values (see

Section 2) of  $\sim 600$  meV (50 nm + 25 °C + 10C) and  $\sim 980$  meV (1 nm + 60 °C + C/2), signifying “strict” and “lenient” mobility specifications, respectively. The calculated  $E_m$ , band gaps (this work), and ESWs (from Chen et al.<sup>24</sup>) are also reported in Table 1. The oxidative limit for  $Mg_{0.5}Ti_2(PO_4)_3$

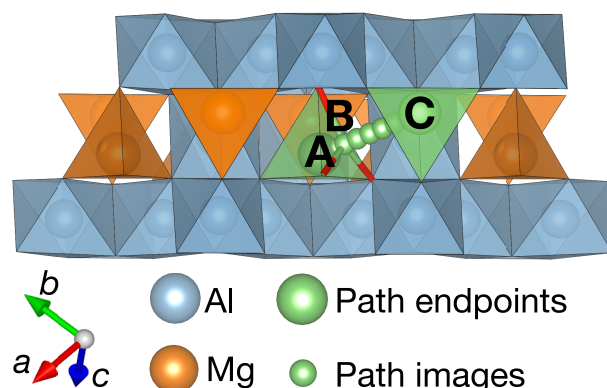
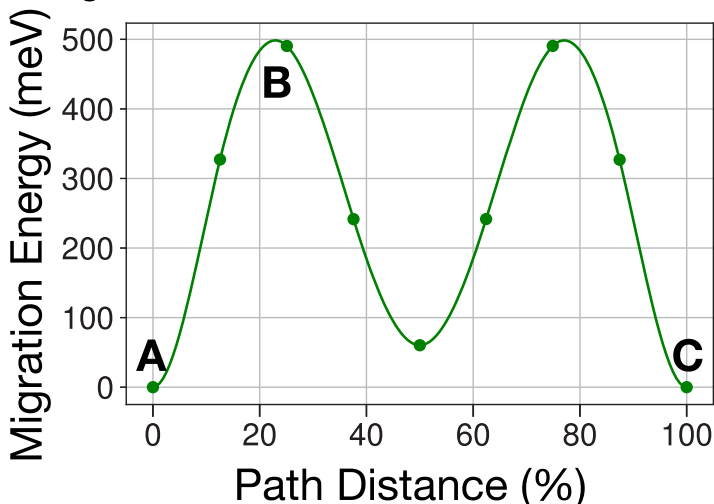
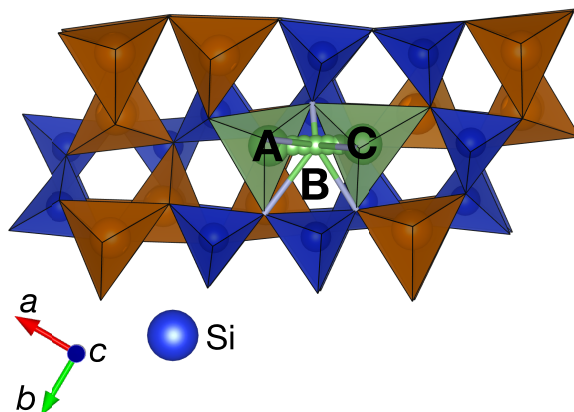
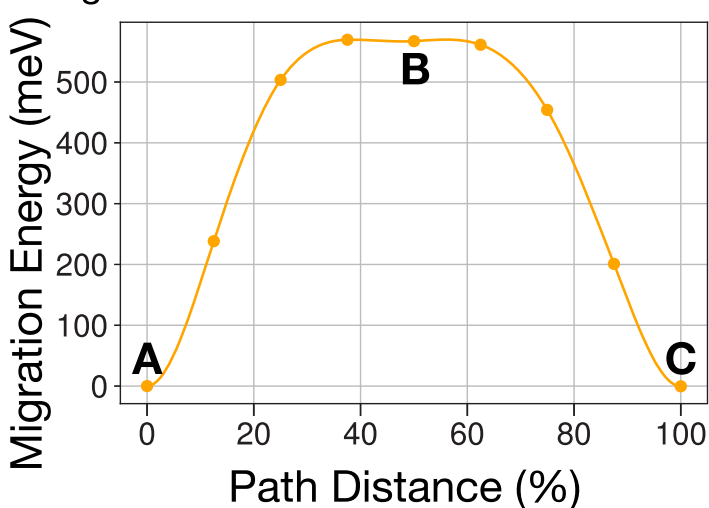
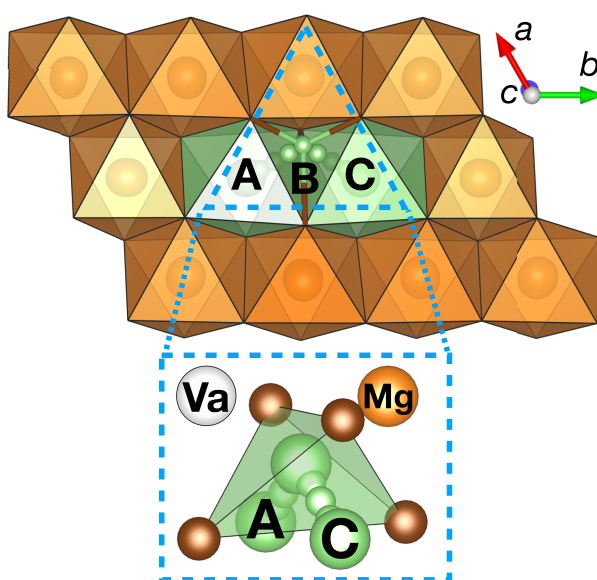
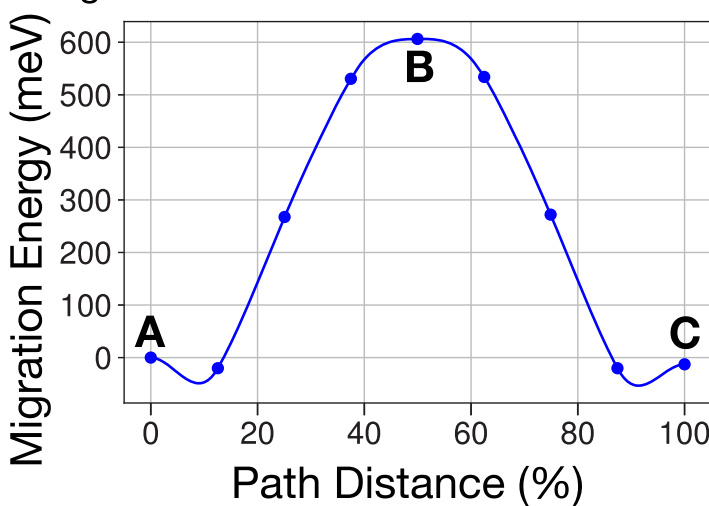
**Table 1. Computed Migration Energy (in meV) of  $Mg^{2+}$  Ions in the Structures Considered<sup>b</sup>**

material	MP/ICSD	ESW	band gap	$E_m$
$Mg_3N_2$	mp-1559	0.80	3.39	655
$MgSiN_2$	mp-3677	1.20	5.35	570
$Mg(BH_4)_2$	mp-1192265	1.25	6.35	448 <sup>a</sup>
$MgH_2$	mp-23711	0.42	4.05	647
$MgB_2$	mp-763	0.05	0.10	1729
$MgB_4$	mp-365	0.07	0.03	504
$MgB_7$	mp-978275	0.41	1.73	1352
$Mg_2Ge$	mp-408	0.21	0.61	414
$Mg_2Si$	mp-1367	0.12	0.83	1284
$Mg_3As_2$	mp-1990	0.52	2.23	534
$Mg_3P_2$	mp-2514	0.52	2.43	560
$MgP_4$	mp-384	0.27	0.69	1563
$MgO$	mp-1265	3.08	6.02	1851
$MgS$	mp-1315	3.39	2.94	943
$MgSe$	mp-1018040	1.26	3.00	950
$MgTe$	mp-1039	0.88	2.79	939
$MgF_2$	mp-1249	5.78	8.70	1123
$MgCl_2$	mp-23210	3.39	6.84	$786 \pm 160$
$MgBr_2$	mp-30034	2.28	4.90	$627 \pm 160$
$MgI_2$	mp-23205	1.60	3.13	$604 \pm 160$
$Mg_{0.5}Ti_2(PO_4)_3$	mp-1043685	3.55	4.07	1105
$MgNb_2O_6$	mp-17953	2.29	4.46	1358
$MgAl_2O_4$	mp-3536	3.13	6.77	491
$MgB_4O_7$	mp-14234	2.74	6.91	2056
$Mg(PO_3)_2$	mp-18620	2.33	7.11	699
$MgP_4O_{11}$	mp-15437	2.24	6.70	3541
$MgS_2O_7$	ICSD 426707	1.93	7.19	1699

<sup>a</sup>Reported barrier should exhibit error higher than  $\pm 50$  meV. <sup>b</sup>The Materials Project mp-IDs or the collection codes from the inorganic crystal structure database (ICSD) are listed for each structure. The ESWs (V vs Mg), as reported in ref 24, and the computed electronic band gaps (in eV) are also listed. Unless explicitly mentioned, the overall accuracy of our migration barriers is  $\pm 50$  meV.

differs from that in ref 24 due to the inclusion of ternary- $TiP_2O_7$  in the ESW calculations of this work. Variation of the calculated migration energies along the migration paths of all materials listed in Table 1 are provided in Supporting Information Section S1. We also evaluated  $E_m$  in a set of metastable polymorphs at the compositions of  $Mg_3P_2$ ,  $Mg_2Si$ ,  $MgSe_2$ , and  $MgTe_2$ , which are displayed in Supporting Information Section S2.

There are several materials that show appropriate Mg mobility under the strict 600 meV criterion, namely,  $MgSiN_2$  (570 meV),  $MgB_4$  (504 meV),  $Mg_2Ge$  (414 meV),  $Mg_3As_2$  (534 meV), and  $Mg_3P_2$  (560 meV) on the anode and  $MgAl_2O_4$  (491 meV) on the cathode. Unsurprisingly, using a lenient threshold of 980 meV, we obtain additional candidates, including  $MgH_2$  (647 meV),  $Mg_3N_2$  (655 meV),  $MgTe$  (939 meV),  $MgSe$  (950 meV),  $MgS$  (943 meV),  $MgI_2$  ( $604 \pm 160$  meV),  $MgBr_2$  ( $627 \pm 160$  meV), and  $MgCl_2$  ( $786 \pm 160$  meV) on the anode and  $Mg(PO_3)_2$  (699 meV) on the cathode. Although we report a low  $E_m$  for  $Mg(BH_4)_2$  ( $\sim 448$  meV), we

**a** MgAl<sub>2</sub>O<sub>4</sub>**b** MgSiN<sub>2</sub>**c** MgBr<sub>2</sub>

**Figure 4.** Migration energies of (a) MgAl<sub>2</sub>O<sub>4</sub>, (b) MgSiN<sub>2</sub>, and (c) MgBr<sub>2</sub> (left) along the calculated migration paths (right). For each migration path shown, the end points are labeled A and C (green polyhedra), the activated state is labeled B (green sphere with bonds), and the images along the path are shown as green spheres. Nonmigrating Mg (orange), Al (light blue), and Si (dark blue) are shown as polyhedra with anions (not shown) at all polyhedral vertices. The inset in c shows the nearest-neighbor octahedral cations (Va = vacuum) of the activated tetrahedral state.

encountered significant challenges in converging the NEB for this material. For example, the ground state structure of  $\text{Mg}(\text{BH}_4)_2$  in the Materials Project (ID: mp-1200811 and space group  $I\bar{a}\bar{3}d$ ) contains 264 atoms within its unit cell, making the computational cost of the NEB calculation prohibitive. Despite using a  $\text{Mg}(\text{BH}_4)_2$  polymorph with a smaller unit cell (mp-1192265, 22 atoms, and  $P\bar{4}n2$  space group), we could converge the elastic band only by using a significantly higher force threshold ( $\sim 0.13 \text{ eV}/\text{\AA}$ ), which increases the error associated with the reported  $E_m$ .

Considering the strict  $E_m^{\max}$ , only  $\text{MgSiN}_2$  has an ESW > 1 V among the anode coatings of Figure 3, with an oxidative stability up to 1.2 V vs Mg metal. Under lenient operating conditions,  $\text{MgI}_2$ ,  $\text{MgBr}_2$ , and  $\text{MgCl}_2$  also become promising anode coatings, with oxidative stabilities up to 1.2, 1.6, and 3.4 V, respectively. On the cathode side,  $\text{MgAl}_2\text{O}_4$  has a large ESW of 3.2 V, with a reductive stability of  $\sim 0.1$  V vs Mg. However, the oxidative stability of  $\text{MgAl}_2\text{O}_4$  is only up to 3.3 V, which indicates that  $\text{MgAl}_2\text{O}_4$  may not be compatible vs higher voltage oxide cathodes, such as  $\text{Mg}_x\text{Cr}_2\text{O}_4$  ( $\sim 3.5$  V)<sup>62</sup> but can still be compatible with lower voltage oxide cathodes, such as  $\text{Mg}_x\text{V}_2\text{O}_5$  ( $\sim 2.5$  V)<sup>63,64</sup> and  $\text{Mg}_x\text{Mn}_2\text{O}_4$  ( $\sim 2.8$  V).<sup>37,65,66</sup> On the other hand,  $\text{Mg}(\text{PO}_3)_2$ , which becomes viable under a lenient  $E_m^{\max}$ , exhibits an ESW of 2.4 V with an oxidative stability up to 4.1 V, signifying compatibility with higher-voltage Mg cathodes. In addition,  $\text{MgSiN}_2$ ,  $\text{MgAl}_2\text{O}_4$ , and  $\text{Mg}(\text{PO}_3)_2$  exhibit large band gaps ( $> 5$  eV) and are good electronic insulators.

In general, there is no correlation between electronic band gaps and Mg migration barriers (Table 1) across chemistries and structures. For example, both  $\text{MgB}_2$  and  $\text{MgB}_4\text{O}_7$  display significant migration barriers ( $> 1700$  meV) while possessing contrasting band gaps of 0.1 and 6.91 eV, respectively. However, within an anion group (e.g., chalcogens), there is a direct correlation between lower band gaps and lower migration barriers. For example, the migration barrier in Mg-chalcogenides varies as  $\text{MgO}$  (1851 meV) >  $\text{MgSe}$  (950 meV) >  $\text{MgS}$  (943 meV) >  $\text{MgTe}$  (939 meV), identical to the variation in band gaps,  $\text{MgO}$  (6.02 eV) >  $\text{MgSe}$  (3.00 eV) >  $\text{MgS}$  (2.94 eV) >  $\text{MgTe}$  (2.79 eV). An analogous correlation can also be found in Mg-pnictides and layered Mg-halides, with barriers and band gaps varying as  $\text{Mg}_3\text{N}_2$  >  $\text{Mg}_3\text{P}_2$  >  $\text{Mg}_3\text{As}_2$  and  $\text{MgCl}_2$  >  $\text{MgBr}_2$  >  $\text{MgI}_2$ , respectively. The decrease in both band gaps and migration barriers moving down the anion group ( $\text{Cl} \rightarrow \text{Br} \rightarrow \text{I}$ ) can be attributed to the larger volume per anion within the structure and the weaker overlap between atomic orbitals.

#### 4.2. Mg Migration Topology of Selected Coating Materials.

The evolution of the migration energies (left) along the calculated migration paths (right) of three promising materials,  $\text{MgAl}_2\text{O}_4$  (a),  $\text{MgSiN}_2$  (b), and  $\text{MgBr}_2$  (c), is displayed in Figure 4. We chose to analyze  $\text{MgAl}_2\text{O}_4$ ,  $\text{MgSiN}_2$ , and  $\text{MgBr}_2$  owing to their low migration barriers ( $< 650$  meV). Also,  $E_m$  for  $\text{MgAl}_2\text{O}_4$  and  $\text{MgSiN}_2$  were calculated using step 4 in Figure 2a, while  $\text{MgBr}_2$  required steps 5–7. Nonmigrating Mg, Al, and Si atoms in Figure 4 are indicated by orange, light blue, and dark blue spheres/polyhedra, respectively. The end-points, labeled “A” and “C” in both the migration energy plot and the migration paths, are shown as green polyhedra. The activated state that sets the migration barrier, labeled “B”, is shown with bonds to nearest-neighbor anions to identify its coordination environment. Anion atoms, which occupy all polyhedral vertices in Figure 4, are not shown for clarity.

$\text{MgAl}_2\text{O}_4$  (Figure 4a) shows a migration energy landscape that is typical of spinel-oxides,<sup>31</sup> where the stable tetrahedral sites (end points) are connected via an intermediate octahedral site (not shown in Figure 4a). The activated site (B in Figure 4a) is the triangular face, i.e., migrating Mg coordinated to three nearby oxygen atoms, between the stable tetrahedral and the intermediate octahedral sites. Thus, Mg migration follows a “4–3–6–3–4” pathway, where the numbers refer to the number of anions that are coordinated to the migrating Mg.  $E_m$  for  $\text{MgAl}_2\text{O}_4$  ( $\sim 491$  meV) is similar to the barriers observed, in the low vacancy limit, for oxide cathode spinels, such as  $\text{MgMn}_2\text{O}_4$  (486 meV),  $\text{MgCr}_2\text{O}_4$  (636 meV),  $\text{MgCo}_2\text{O}_4$  (520 meV), and  $\text{MgNi}_2\text{O}_4$  (485 meV),<sup>58</sup> signifying possible compatibility (i.e., similar barriers + lattice) with cathode spinels. Interestingly, the intermediate octahedral site in  $\text{MgAl}_2\text{O}_4$  is unstable by only  $\sim 60$  meV compared to the end-point tetrahedral sites, and the low energy difference between the two sites may contribute to the low migration barrier.<sup>3</sup>

$\text{MgSiN}_2$  (Figure 4b) shows a migration path with stable tetrahedral sites and a 5-coordinated square pyramid as the activated site. Thus, Mg migrates via a 4–3–5–3–4 pathway, similar to topology of  $\delta\text{-V}_2\text{O}_5$ ,<sup>63,67</sup> and exhibits small coordination changes along the path, which may contribute to the low barrier (570 meV). Additionally,  $\text{N}^{3-}$  in  $\text{MgSiN}_2$  bonds more covalently than  $\text{O}^{2-}$  does, which can result in lower barriers via electrostatic shielding of the  $\text{Mg}^{2+}$ . Indeed, Mg-containing ternary  $\text{Se}^{2-}$  and  $\text{S}^{2-}$  spinels, which bond more covalently than  $\text{O}^{2-}$ , typically exhibit lower  $E_m$  than analogous ternary oxide spinels.<sup>12</sup>

In Figure 4c,  $\text{MgBr}_2$  exhibits a barrier of  $\sim 627$  meV, where the Mg migrates across octahedral end points through an activated, face-sharing tetrahedral site. Thus, the Mg migrates via a 6–3–4–3–6 mechanism, analogous to ionic migration in ordered, close-packed, layered oxides, such as Li in  $\text{LiCoO}_2$ <sup>68</sup> and Mg in  $\text{MgNiO}_2$ .<sup>31</sup> Note that both  $\text{MgCl}_2$  and  $\text{MgI}_2$  exhibit identical migration pathways compared to  $\text{MgBr}_2$ . Importantly, layered Mg-halides exhibit significantly lower migration barriers ( $< 800$  meV, Table 1) than  $\text{MgNiO}_2$  ( $> 1000$  meV<sup>31</sup>), which can be attributed to electrostatic interactions. For example, in  $\text{MgNiO}_2$  (or analogous ordered, close-packed, layered oxides), the activated tetrahedron is face-shared with two nonmigrating cation-occupied ( $\text{Ni}^{3+/2+}$ ) octahedra, resulting in significant electrostatic destabilization, i.e., high energy due to strong electrostatic repulsion and higher migration barriers. On the other hand, the activated tetrahedral site in layered Mg-halides (inset of Figure 4c) shares one face with a nonmigrating  $\text{Mg}^{2+}$ -occupied octahedron (which contributes to electrostatic destabilization) and one face with the vacuum (Va) between the halide layers (which does not contribute to electrostatic destabilization), since layers of  $\text{MgBr}_2$  are bonded via van der Waals interactions. Thus, the reduced electrostatic destabilization lowers the energy of the activated tetrahedral site and reduces the  $E_m$  in  $\text{MgBr}_2$  compared to  $\text{MgNiO}_2$ . An alternative 6–2–6 mechanism, with Mg migrating through the shared edge of the  $\text{MgBr}_6$  end points, can also be envisioned, but such a migration mechanism will require higher barriers, as previously demonstrated in  $\text{MgNiO}_2$ <sup>31</sup> and  $\text{Mg}_2\text{Mo}_3\text{O}_8$ .<sup>69</sup>

#### 4.3. Mg-Vacancy Formation in Selected Coating Materials.

While  $E_m$  controls how likely it is for a Mg diffusion carrier to migrate, there should be a sufficient concentration<sup>70</sup> of Mg vacancies (or other diffusion carriers) within the bulk to facilitate Mg transport in the material.

**Table 2.** Computed Formation Energy (in eV) of Mg Vacancies in Selected Coating Materials<sup>a</sup>

defect	q	gap	$E^f[\text{Mg}^q]$						$\epsilon(0/2-)$	
			$\mu_{\text{Mg}} = \mu_{\text{Mg}}^{\text{red}}$			$\mu_{\text{Mg}} = \mu_{\text{Mg}}^{\text{oxi}}$				
			@VBM	@ $E_{\text{Fermi}}^{\text{eq}}$	@CBM	@VBM	@ $E_{\text{Fermi}}^{\text{eq}}$	@CBM		
$\text{MgAl}_2\text{O}_4$										
$V''_{\text{Mg}}$	-2	5.13	9.22	9.11	-1.05	2.96	2.85	-7.31	1.07	
	0		7.08			0.82				
$\text{MgSiN}_2$										
$V''_{\text{Mg}}$	-2	4.02	6.02	6.01	-2.02	3.62	3.61	-4.42	0.71	
	0		4.61			2.21				
$\text{MgBr}_2$										
$V''_{\text{Mg}}$	-2	4.47	6.74	6.49	-2.20	2.18	1.93	-6.76	0.93	
	0		4.89			0.33				

<sup>a</sup>The formation energies are calculated at  $\mu_{\text{Mg}}$  corresponding to the reductive ( $\mu_{\text{Mg}}^{\text{red}}$ ) and oxidative ( $\mu_{\text{Mg}}^{\text{oxi}}$ ) stability limits, respectively, of each material. The range of  $E_{\text{Fermi}}$  is set by the valence band maximum (VBM) and the conduction band minimum (CBM) of the pristine bulk structure.  $E_{\text{Fermi}}^{\text{eq}}$  is the equilibrium Fermi energy in the defect-free bulk. Band gaps listed (in eV) are calculated using the PBE functional.  $\epsilon$  is the acceptor transition level of  $V_{\text{Mg}}$  (in eV). Schematic of the  $E_{\text{corr}}$  schemes used is provided in Supporting Information Section S4.

Hence, we evaluated the energy required to form a Mg vacancy ( $E^f[\text{Mg}^q]$ ) within  $\text{MgAl}_2\text{O}_4$ ,  $\text{MgSiN}_2$ , and  $\text{MgBr}_2$  (Section 4.2 and Figure 4), with Table 2 listing the calculated values. In computing  $E^f[\text{Mg}^q]$ , we considered two charge states of the Mg vacancy: (i) neutral ( $q = 0$ ),  $V_{\text{Mg}}^{\times}$  and (ii) charge-compensated ( $q = -2$ ),  $V''_{\text{Mg}}$ . We calculate  $E^f[\text{Mg}^q]$  at Mg chemical potentials signifying the oxidative ( $\mu_{\text{Mg}}^{\text{oxi}}$ ) and reductive ( $\mu_{\text{Mg}}^{\text{red}}$ ) stability limits for each material (see Figure 3), specifically 0.1–3.23 V for  $\text{MgAl}_2\text{O}_4$ , 0–1.20 V for  $\text{MgSiN}_2$ , and 0–2.28 V for  $\text{MgBr}_2$ .<sup>24</sup> Also, we consider the range of Fermi energies spanning across the valence band maximum (VBM) and the conduction band minimum (CBM) within the bulk material.  $E_{\text{Fermi}}^{\text{eq}}$  is the equilibrium Fermi energy in the defect-free bulk, as calculated by DFT, which lies between the VBM and CBM in nonmetals and is relevant for an as-synthesized coating material. Band gaps in Table 2 are calculated with PBE, to be consistent with the total energies used in eq 3, and are lower than the HSE06-calculated values in Table 1.  $\epsilon(0/2-)$  is the acceptor transition level within each material, which is the  $E_{\text{Fermi}}$  at which  $E^f[\text{Mg}^{2-}] = E^f[\text{Mg}^0]$ . All  $\epsilon$  values are listed (in eV) with respect to the VBM of the corresponding material. Note that in all cases considered, the values of  $E_{\text{Fermi}}^{\text{eq}}$  are only slightly larger (<0.2 eV) than the VBM and thus the  $E^f[\text{Mg}^{2-}]$  computed @ $E_{\text{Fermi}}^{\text{eq}}$  are similar to the values @VBM.

In general, the values of  $E^f[\text{Mg}^q]$  in all three materials and in all the charge states are higher at  $\mu_{\text{Mg}}^{\text{red}}$  than  $\mu_{\text{Mg}}^{\text{oxi}}$ , which is in line with the higher availability of Mg under reducing (anode-like) than under oxidizing (cathode-like) conditions. For example,  $E^f[\text{Mg}^0]$  for  $\text{MgAl}_2\text{O}_4$  at  $\mu_{\text{Mg}}^{\text{red}}$  (7.08 eV) is higher by 6.26 eV than at  $\mu_{\text{Mg}}^{\text{oxi}}$  (0.82 eV), which is equivalent to twice the range of the ESW of  $\text{MgAl}_2\text{O}_4$  (3.13 V, Figure 3). Thus, all coating materials in Table 2 should exhibit a higher concentration of Mg vacancies at their oxidizing (cathode or electrolyte) than at their reducing (anode) interface, which sets a Mg concentration gradient across the coating layer and should facilitate Mg transport away from the anode and toward the cathode during discharge. Additionally,  $E^f[\text{Mg}^{2-}]$  is higher at the VBM than the CBM for all materials and  $\mu_{\text{Mg}}$  considered, which is expected given that negatively charged defects become more likely as the electron chemical potential (i.e.,  $E_{\text{Fermi}}$ ) increases toward the conduction band (i.e., reducing conditions). The decrease in  $E^f[\text{Mg}^{2-}]$  from VBM to CBM is equivalent to twice the band gap for each material, corresponding to a charge of

-2. Also, @VBM,  $E^f[\text{Mg}^q]$  for  $q = 0$  is consistently lower than  $q = -2$  for all structures and  $\mu_{\text{Mg}}$  indicating that neutral Mg vacancies are likely to form at lower  $E_{\text{Fermi}}$  compared to charge-compensated Mg vacancies. Particularly, the materials in Table 2 should form  $V_{\text{Mg}}^{\times}$  at the oxidizing (cathode or electrolyte) interface since the Fermi energy is typically lower (and approaches VBM) at the cathode/electrolyte during discharge.<sup>34</sup>

$E^f[\text{Mg}^0]$  @ $E_{\text{Fermi}}^{\text{eq}}$  follows the trend  $\text{MgAl}_2\text{O}_4$  (9.11 eV) >  $\text{MgBr}_2$  (4.89 eV) >  $\text{MgSiN}_2$  (4.61 eV), highlighting that the as-synthesized materials will exhibit  $V_{\text{Mg}}$  concentrations in the order  $\text{MgAl}_2\text{O}_4 < \text{MgBr}_2 < \text{MgSiN}_2$ . Given that  $V''_{\text{Mg}}$  is more stable than  $V_{\text{Mg}}^{\times}$  at  $E_{\text{Fermi}}$  beyond 1.07 eV for  $\text{MgAl}_2\text{O}_4$  (within a gap of 5.13 eV), 0.71 eV for  $\text{MgSiN}_2$  (gap = 4.02 eV), and 0.93 eV for  $\text{MgBr}_2$  (gap = 4.47 eV), we predict all materials in Table 2 to exhibit relatively “shallow” acceptor levels ( $\epsilon$ ) within their band gaps. Thus,  $\text{MgAl}_2\text{O}_4$ ,  $\text{MgSiN}_2$ , and  $\text{MgBr}_2$  are likely to form charge-compensated Mg vacancies, particularly at their reducing interfaces with anodes, where  $E_{\text{Fermi}}$  is likely to approach the CBM. Although negative values of  $E^f[\text{Mg}^{2-}]$ , particularly as  $E_{\text{Fermi}} \rightarrow \text{CBM}$ , are indicative of bulk instability for all materials in Table 2 under highly reducing conditions, the formation of such defects will depend on the actual Fermi level at the anode||coating interface.

## 5. DISCUSSION

Using DFT calculations coupled with the NEB method, we have evaluated several binary, ternary, and quaternary compounds as potential anode/cathode coatings for high energy density Mg batteries. Protective coatings form an important component in the practical realization of Mg batteries due to the lack of stable (solid/liquid) electrolytes that are compatible with both high-voltage oxide cathodes and a Mg metal anode. Using a strict mobility threshold (600 meV, Figure 1) based on practical battery operating conditions, we identified  $\text{MgSiN}_2$ ,  $\text{Mg}_2\text{Ge}$ ,  $\text{Mg}_3\text{As}_2$ , and  $\text{Mg}_3\text{P}_2$  as potential anode coatings and  $\text{MgAl}_2\text{O}_4$  as a promising cathode coating (Figure 3).  $\text{MgB}_4$  also showed a low migration barrier ( $E_m \sim 504$  meV) but may not be suitable as an anode coating since it exhibits a small ESW (~0.05 V) and is not stable against Mg metal (reductive stability of ~0.05 V). Additionally, we identified candidates that can function under more lenient operating conditions (980 meV), including  $\text{MgH}_2$ ,  $\text{Mg}_3\text{N}_2$ ,  $\text{MgTe}$ ,  $\text{MgSe}$ ,  $\text{MgS}$ ,  $\text{MgI}_2$ ,  $\text{MgBr}_2$ , and  $\text{MgCl}_2$  on the anode and

$\text{Mg}(\text{PO}_3)_2$  on the cathode. Finally, combining mobility and stability ( $\text{ESW} > 1 \text{ V}$ ) requirements, we suggest  $\text{MgSiN}_2$ ,  $\text{MgSe}$ ,  $\text{MgS}$ ,  $\text{MgI}_2$ , and  $\text{MgBr}_2$  as promising anode coatings and  $\text{MgAl}_2\text{O}_4$  and  $\text{Mg}(\text{PO}_3)_2$  as possible cathode coatings.

The coatings with the highest oxidative stabilities in **Figure 3** are  $\text{MgF}_2$  (5.8 V),  $\text{MgP}_4\text{O}_{11}$  (4.5 V), and  $\text{MgS}_2\text{O}_7$  (4.5 V), which are also large gap ( $>6.5 \text{ eV}$ ) electronic insulators (**Table 1**). Particularly,  $\text{MgF}_2$  is stable against Mg-metal and shows the largest ESW (5.8 V) among Mg-containing compounds.<sup>24</sup> However, these materials cannot be considered as coatings due to their high Mg migration barriers ( $\text{MgF}_2 \sim 1123 \text{ meV}$ ,  $\text{MgP}_4\text{O}_{11} \sim 3541$ , and  $\text{MgS}_2\text{O}_7 \sim 1699$ ), which exceed even the lenient  $E_m^{\max}$  threshold. Thus, our work highlights the importance of considering potential kinetic limitations when identifying coating candidates. Also, we have restricted our work here to structures involving a unique anion (i.e., halides, chalcogenides, pnictides, etc.), but it would be interesting to evaluate Mg compounds/structures with mixed anions (e.g., oxy-sulfides, oxy-halides, oxy-nitrides, etc.) for coating applications since having multiple anions will provide an additional handle to calibrate the stability, mobility, and electronic properties. Further, we have only evaluated the properties of stoichiometric Mg compounds in this work. The possible existence and role of significant Mg off-stoichiometry at the anode (Mg excess) and cathode (Mg deficiency) interfaces will be an important area for future studies.

One important assumption made in this work is that long-range ionic diffusion in coating materials follows a random-walk model without any appreciable degree of correlation between local migration events, i.e.,  $f \sim 1$  in **eq 1**. While several cathodes and solid electrolytes indeed obey random-walk diffusion, as indicated by the robust agreement between experimentally measured and theoretically predicted migration barriers,<sup>55</sup> it remains to be seen if any degree of correlation exists in coating materials. Computationally expensive AIMD or kinetic Monte Carlo simulations can provide some theoretical evidence for correlation during diffusion (if it exists), while experimental measurements, such as impedance spectroscopy (IS) and/or nuclear magnetic resonance (NMR), can also be used to probe correlation. Such extensive computational simulations and/or experimental measurements can also be used to infer the ease of Mg diffusion along grain boundaries within the coating layer, which can significantly alter the overall Mg transport.<sup>71,72</sup>

We found that the layered  $\text{MgX}_2$  structures (X = Cl, Br, and I) exhibit significant structural distortion upon addition of a jellium background, which is typically used for charge compensation in periodic boundary DFT calculations. To circumvent this limitation, we devised a three-step procedure (steps 5–7, **Figure 2a**) to calculate Mg migration barriers, which can result in an error of  $\sim 160 \text{ meV}$  (**Figure 2c**). While the DFT+NEB workflow (**Figure 2a**) can be generalized to evaluate ionic transport in other material chemistries as well, more theoretical studies are required to further develop alternate strategies to model local charge imbalances and to better quantify errors. In particular, experimental measurements of Mg migration barriers, using variable temperature (VT) IS or VT-NMR, would be useful to validate and improve the theoretical description of candidate coating materials.

Analyzing the Mg migration topology of three distinct candidates with  $E_m < 650 \text{ meV}$  (**Figure 4**), we found similarities between  $\text{MgAl}_2\text{O}_4$  and oxide cathode spinels,  $\text{MgSiN}_2$  and  $\delta\text{-V}_2\text{O}_5$ , and  $\text{MgBr}_2$  and close-packed layered

oxide cathodes. In particular,  $\text{MgAl}_2\text{O}_4$  should exhibit low lattice mismatch with oxide spinel cathodes, such as spinel- $\text{Mg}_x\text{Mn}_2\text{O}_4$ , and also has a similar  $E_m$  at the low vacancy limit, highlighting its suitability as a cathode coating. However,  $\text{MgAl}_2\text{O}_4$  against Mg-metal is likely to decompose further into Al and  $\text{MgO}^{24}$  and is thus unlikely to be suitable as an anode coating.

On the other hand,  $\text{MgSiN}_2$  (**Figure 4b**) is stable against Mg metal (hence a potential anode coating) but shows a low oxidative stability ( $\sim 1.2 \text{ V}$ ) and may not be compatible with low voltage sulfide cathodes (e.g.,  $\text{Mg}_x\text{Mo}_6\text{S}_8$  and  $\text{Mg}_x\text{Ti}_2\text{S}_4$ <sup>1,38</sup>) due to differences in structure and anion ( $\text{N}^{3-}$  vs  $\text{S}^{2-}$ ). The low  $E_m$  in  $\text{MgSiN}_2$  can be attributed to the small changes in the coordination environment along the migration pathway as well as the covalent bonding exhibited by  $\text{N}^{3-}$  compared to  $\text{O}^{2-}$ . The recent demonstration that theoretically predicted novel ternary nitride compounds can be experimentally synthesized<sup>73</sup> holds promise in the identification of new Mg-containing nitrides with appreciable thermodynamic stability and Mg mobility to function as coating materials.

Due to the lack of atomic occupation in the interlayer spacing, layered Mg-halides, i.e.,  $\text{MgCl}_2$ ,  $\text{MgBr}_2$  (**Figure 4c**), and  $\text{MgI}_2$ , exhibit an interesting structural motif not usually observed in other Mg compounds. While close-packed layered compounds (e.g.,  $\text{MgNiO}_2$ ) are typically expected to yield larger Mg migration barriers due to strong electrostatic interactions and the octahedral coordination preference of Mg,<sup>31</sup> the lack of electrostatic destabilization of the activated tetrahedral site significantly lowers the barrier in  $\text{MgBr}_2$ . Such reduction in migration barriers, by lowering electrostatic interactions, has been demonstrated in disordered, close-packed, layered, Li-excess oxide cathodes.<sup>74</sup> Thus, layered/close-packed structures that can lower the electrostatic destabilization of the activated site, via cation disorder, for example, might be a promising motif to identify novel materials with facile Mg mobility.

In the calculation of diffusivity (**eq 1**), it is generally assumed that diffusion carriers are already present in the coating materials during battery operation. These defects can result from either a transfer of Mg at the coating||electrode interface or due to intrinsic defects. However, if the formation of diffusion carriers has a significant energy penalty ( $E^f[\text{Mg}^q]$ ), then the Mg diffusivity will drop by  $\exp\left(-\frac{E^f[\text{Mg}^q]}{k_B T}\right)$  compared to estimates using only  $E_m$  (**eq 1**). In order to assess whether the formation energies of the Mg vacancies will limit Mg transport, we calculated  $E^f[\text{Mg}^q]$  in  $\text{MgAl}_2\text{O}_4$ ,  $\text{MgSiN}_2$ , and  $\text{MgBr}_2$ . We find that the vacancy formation energies in all three materials (**Table 2**) are lower under oxidizing ( $\mu_{\text{Mg}}^{\text{ox}}$  and @ VBM) than reducing ( $\mu_{\text{Mg}}^{\text{red}}$  and @CBM), signifying a higher concentration of Mg vacancies at the oxidizing interface compared to the reducing interface, which can facilitate Mg transport during battery discharge. Additionally, given that the electron chemical potential ( $E_{\text{Fermi}}$ ) approaches the VBM (CBM) at the oxidizing (reducing) interface, neutral (charge-compensated) Mg vacancies will dominate at the oxidizing (reducing) interface.

At the anode||coating interface (and @CBM), the negative values of  $E^f[\text{Mg}^{2-}]$  for all materials in **Table 2**, which corresponds to the transfer of  $\text{Mg}^{2+}$  across the interface, highlights potential instability of the coatings. Note that we evaluated the anodic stability limit (**Figure 3**) across all materials for Mg-atom transfer (i.e.,  $\text{Mg}^{2+} + 2\text{e}^-$ ), and the

exchange of only  $Mg^{2+}$  (i.e., charge transfer) can indeed lead to large concentrations of  $V''_{Mg}$  under reducing conditions, eventually destabilizing the coating. In general, charge transfer across an interface (e.g.,  $Mg^{2+}$  exchange leading to formation/annihilation of  $V''_{Mg}$ ) depends on the Fermi level at the interface ( $E_{Fermi}^{int}$ ), which is different from the equilibrium Fermi level within the bulk coating material.  $E_{Fermi}^{int}$  depends on the alignment of the bands between the bulk components (e.g., coating and anode), band bending at the interface, and any applied potential.<sup>75</sup>

Theoretically calculating  $E_{Fermi}^{int}$  typically requires an explicit model of the interface involving hundreds of atoms and adds significant computational expense. Thus, rigorous estimation of  $E_{Fermi}^{int}$  and the resultant  $E'[\text{Mg}^{2-}]$ , will be required to predict if the coating materials considered here remain stable for a charge transfer process at the anode or the cathode. Another consideration is that any applied over/underpotential affects  $E_{Fermi}^{int}$  and, consequently, the concentration of  $V''_{Mg}$ . As a result, if there are insufficient diffusion carriers in a given coating material, a potential solution is to apply an appropriate over/underpotential, in addition to the over/underpotentials applied to compensate electronic and/or ionic resistance contributions in electrochemical setups. Hence, we expect poor Mg migration, not the lack of diffusion carriers, to be the main bottleneck in the development of coating materials for Mg batteries.

Although there is no broad association between Mg migration barriers and electronic band gaps, barriers do decrease monotonically with decreasing band gaps within an anion group, likely due to trends in volume per anion and atomic orbital overlap (Table 1). In general, higher electronic conductivity in coatings compared to electrolytes is detrimental to electrolyte stability and can cause battery self-discharge.<sup>23</sup> Two candidates with relatively low  $Mg^{2+}$  migration barriers (<600 meV), namely,  $MgB_4$  (band gap ~0.03 eV) and  $Mg_2Ge$  (~0.61 eV), have a small band gap (<1 eV, high electronic conductivity) and small ESW (<1 V, low ability to accommodate a large chemical potential difference). Hence,  $MgB_4$  and  $Mg_2Ge$  will conduct both electrons and  $Mg^{2+}$ , causing electrolyte instability, and are not suitable as coating materials. There are also candidates with sufficient Mg mobility and ESW (>1 V) but with low band gaps (<2 eV), such as  $MgSiN_2$ ,  $MgSe$ , and  $MgI_2$ , which can result in higher electronic conductivities within the coating than the electrolyte. However, using thicker layers of  $MgSiN_2$ ,  $MgSe$ , and  $MgI_2$  as anode coatings may mitigate the influence of electronic conductivity and accommodate electrolytes with narrow ESWs.

Ideally, coatings in Mg batteries should (i) be inexpensive, (ii) involve simple equipment, and (iii) not alter the composition/properties of electrodes and electrolytes. Several strategies exist to introduce coating materials onto electrodes in Li-ion batteries, as summarized recently by Culver et al.<sup>35</sup> Inexpensive and simpler techniques include wet and chemical spray coating, while expensive and advanced techniques include ALD, PLD, and chemical vapor deposition. In general, the cost of a coating increases dramatically if thinner (subnanometer) layers are to be formed.<sup>35</sup> It remains to be seen if coating techniques routinely applied to Li-ion batteries can be translated directly to Mg (and multivalent) batteries. In particular, the low tolerance of Mg battery components toward oxygen contamination may represent a significant challenge in the preparation of *ex situ* coated electrodes.

## 6. CONCLUSION

In this study, we use density functional theory calculations to identify protective coating materials for Mg batteries, a potential, beyond Li-ion, high energy density secondary electrochemical storage system. Based on a set of minimal ionic mobility requirements in potential coatings, which are applicable to all intercalation battery systems, we found a wide variety of candidate coating materials. For example, using a strict mobility threshold (600 meV), we identified  $MgSiN_2$ ,  $MgB_4$ ,  $Mg_2Ge$ ,  $Mg_3As_2$ ,  $Mg_3P_2$ , and  $MgAl_2O_4$  as potential coatings, while using a lenient threshold (980 meV) extended our candidate set to include  $MgH_2$ ,  $Mg_3N_2$ ,  $MgTe$ ,  $MgSe$ ,  $MgS$ ,  $MgI_2$ ,  $MgBr_2$ ,  $MgCl_2$ , and  $Mg(PO_3)_2$ . Among the aforementioned candidates,  $MgAl_2O_4$  and  $Mg(PO_3)_2$  should be compatible against oxide cathodes (>3 V vs Mg), while  $MgSiN_2$ ,  $MgS$ ,  $MgSe$ ,  $MgBr_2$ , and  $MgI_2$  should be compatible with the Mg metal anode and exhibit reasonable ESW (>1 V). Upon inspecting the Mg migration topology in a subset of the candidates listed above, we observed similarities with other migration pathways, such as spinels,  $\delta\text{-V}_2\text{O}_5$ , and close-packed layered structures. Further, we expect that layered frameworks, similar to  $MgX_2$  (X = Cl, Br, and I), can exhibit reasonable Mg migration barriers due to the lower electrostatic destabilization from the vacuum interlayer that face-shares with the activated site during migration. Finally, we suggest careful and dedicated experimental measurements combined with advanced characterization techniques to further validate our theoretical predictions and progress toward practical Mg batteries.

## ■ ASSOCIATED CONTENT

### S Supporting Information

The Supporting Information is available free of charge on the ACS Publications website at DOI: [10.1021/acs.chemmater.9b02692](https://doi.org/10.1021/acs.chemmater.9b02692).

All the migration barriers and their migration paths for all compounds, migration barriers at varying supercell size for single-vacancy migration in  $MgS$ , and computational details on the calculation of the vacancy defect formation energy (PDF)

## ■ AUTHOR INFORMATION

### Corresponding Authors

\*(G.S.G.) E-mail: [gautam91@princeton.edu](mailto:gautam91@princeton.edu).

\*(P.C.) E-mail: [pcanepa@nus.edu.sg](mailto:pcanepa@nus.edu.sg).

### ORCID ®

Tina Chen: [0000-0003-0254-8339](https://orcid.org/0000-0003-0254-8339)

Gopalakrishnan Sai Gautam: [0000-0002-1303-0976](https://orcid.org/0000-0002-1303-0976)

Pieremanuele Canepa: [0000-0002-5168-9253](https://orcid.org/0000-0002-5168-9253)

### Notes

The authors declare no competing financial interest.

## ■ ACKNOWLEDGMENTS

P.C. acknowledges support from the Singapore Ministry of Education Academic Fund Tier 1 (R-284-000-186-133). T.C. is supported by the National Science Foundation Graduate Research Fellowship under Grant No. DGE 1106400. The computational work for this article was performed on resources of the National Supercomputing Centre, Singapore (<https://www.nscc.sg>), and the National Science Foundations Extreme Science and Engineering Development Environment (XSEDE) supercomputer Stampede2, through allocation TG-

DMR970008S, which is supported by National Science Foundation Grant Number ACI-1548562.

## ■ REFERENCES

- (1) Aurbach, D.; Lu, Z.; Schechter, A.; Gofer, Y.; Gizbar, H.; Turgeman, R.; Cohen, Y.; Moshkovich, M.; Levi, E. Prototype systems for rechargeable magnesium batteries. *Nature* **2000**, *407*, 724–727.
- (2) Yoo, H. D.; Shterenberg, I.; Gofer, Y.; Gershinsky, G.; Pour, N.; Aurbach, D. Mg rechargeable batteries: an on-going challenge. *Energy Environ. Sci.* **2013**, *6*, 2265.
- (3) Canepa, P.; Sai Gautam, G.; Hannah, D. C.; Malik, R.; Liu, M.; Gallagher, K. G.; Persson, K. A.; Ceder, G. Odyssey of Multivalent Cathode Materials: Open Questions and Future Challenges. *Chem. Rev.* **2017**, *117*, 4287–4341.
- (4) Davidson, R.; Verma, A.; Santos, D.; Hao, F.; Fincher, C.; Xiang, S.; Van Buskirk, J.; Xie, K.; Pharr, M.; Mukherjee, P. P.; Banerjee, S. Formation of Magnesium Dendrites during Electrodeposition. *ACS Energy Letters* **2019**, *4*, 375–376.
- (5) Ding, M. S.; Diemant, T.; Behm, R. J.; Passerini, S.; Giffin, G. A. Dendrite Growth in Mg Metal Cells Containing Mg(TFSI)<sub>2</sub>/Glyme Electrolytes. *J. Electrochem. Soc.* **2018**, *165*, A1983–A1990.
- (6) Ponrouch, A.; Bitenc, J.; Dominko, R.; Lindahl, N.; Johansson, P.; Palacin, M. Multivalent rechargeable batteries. *Energy Storage Materials* **2019**, *20*, 253–262.
- (7) Muldoon, J.; Bucur, C. B.; Gregory, T. Quest for Nonaqueous Multivalent Secondary Batteries: Magnesium and Beyond. *Chem. Rev.* **2014**, *114*, 11683–11720.
- (8) Ling, C.; Zhang, R.; Arthur, T. S.; Mizuno, F. How General is the Conversion Reaction in Mg Battery Cathode: A Case Study of the Magnesiation of  $\alpha\text{-MnO}_2$ . *Chem. Mater.* **2015**, *27*, 5799–5807.
- (9) Ling, C.; Zhang, R. Manganese Dioxide As Rechargeable Magnesium Battery Cathode. *Front. Energy Res.* **2017**, *5*, 30.
- (10) Xu, K. Electrolytes and Interphases in Li-Ion Batteries and Beyond. *Chem. Rev.* **2014**, *114*, 11503–11618.
- (11) MacNeil, D.; Lu, Z.; Chen, Z.; Dahn, J. A comparison of the electrode/electrolyte reaction at elevated temperatures for various Li-ion battery cathodes. *J. Power Sources* **2002**, *108*, 8–14.
- (12) Canepa, P.; Bo, S.-H.; Sai Gautam, G.; Key, B.; Richards, W. D.; Shi, T.; Tian, Y.; Wang, Y.; Li, J.; Ceder, G. High magnesium mobility in ternary spinel chalcogenides. *Nat. Commun.* **2017**, *8*, 1759.
- (13) Martinolich, A. J.; Lee, C.-W.; Lu, I.-T.; Bevilacqua, S. C.; Peefer, M. B.; Bernardi, M.; Schleife, A.; See, K. A. Solid-State Divalent Ion Conduction in ZnP<sub>3</sub>. *Chem. Mater.* **2019**, *31*, 3652–3661.
- (14) Wang, L.-P.; Zhao-Karger, Z.; Klein, F.; Chable, J.; Braun, T.; Schür, A. R.; Wang, C.-R.; Guo, Y.-G.; Fichtner, M. MgSc<sub>2</sub>Se<sub>4</sub>-A Magnesium Solid Ionic Conductor for All-Solid-State Mg Batteries? *ChemSusChem* **2019**, *12*, 2286–2293.
- (15) Canepa, P.; Sai Gautam, G.; Broberg, D.; Bo, S.-H.; Ceder, G. Role of Point Defects in Spinel Mg Chalcogenide Conductors. *Chem. Mater.* **2017**, *29*, 9657–9667.
- (16) Goodenough, J. B.; Kim, Y. Challenges for Rechargeable Li Batteries. *Chem. Mater.* **2010**, *22*, 587–603.
- (17) Xiao, Y.; Miara, L. J.; Wang, Y.; Ceder, G. Computational Screening of Cathode Coatings for Solid-State Batteries. *Joule* **2019**, *3*, 1252–1275.
- (18) Chen, Z.; Qin, Y.; Amine, K.; Sun, Y.-K. Role of surface coating on cathode materials for lithium-ion batteries. *J. Mater. Chem.* **2010**, *20*, 7606.
- (19) Myung, S.-T.; Izumi, K.; Komaba, S.; Sun, Y.-K.; Yashiro, H.; Kumagai, N. Role of Alumina Coating on Li-Ni-Co-Mn-O Particles as Positive Electrode Material for Lithium-Ion Batteries. *Chem. Mater.* **2005**, *17*, 3695–3704.
- (20) Aykol, M.; Kim, S.; Hegde, V. I.; Snydacker, D.; Lu, Z.; Hao, S.; Kirklin, S.; Morgan, D.; Wolverton, C. High-throughput computational design of cathode coatings for Li-ion batteries. *Nat. Commun.* **2016**, *7*, 13779.
- (21) Myung, S.-T.; Izumi, K.; Komaba, S.; Yashiro, H.; Bang, H. J.; Sun, Y.-K.; Kumagai, N. Functionality of Oxide Coating for Li[Li<sub>0.05</sub>Ni<sub>0.4</sub>Co<sub>0.15</sub>Mn<sub>0.4</sub>]O<sub>2</sub> as Positive Electrode Materials for Lithium-Ion Secondary Batteries. *J. Phys. Chem. C* **2007**, *111*, 4061–4067.
- (22) Qian, D.; Xu, B.; Cho, H.-M.; Hatsukade, T.; Carroll, K. J.; Meng, Y. S. Lithium Lanthanum Titanium Oxides: A Fast Ionic Conductive Coating for Lithium-Ion Battery Cathodes. *Chem. Mater.* **2012**, *24*, 2744–2751.
- (23) Nakamura, T.; Amezawa, K.; Kulisch, J.; Zeier, W. G.; Janek, J. Guidelines for All-Solid-State Battery Design and Electrode Buffer Layers Based on Chemical Potential Profile Calculation. *ACS Appl. Mater. Interfaces* **2019**, *11*, 19968–19976.
- (24) Chen, T.; Ceder, G.; Sai Gautam, G.; Canepa, P. Evaluation of Mg Compounds as Coating Materials in Mg Batteries. *Front. Chem.* **2019**, *7*, 24.
- (25) Richards, W. D.; Miara, L. J.; Wang, Y.; Kim, J. C.; Ceder, G. Interface Stability in Solid-State Batteries. *Chem. Mater.* **2016**, *28*, 266–273.
- (26) Snydacker, D. H.; Hegde, V. I.; Wolverton, C. Electrochemically Stable Coating Materials for Li, Na, and Mg Metal Anodes in Durable High Energy Batteries. *J. Electrochem. Soc.* **2017**, *164*, A3582–A3589.
- (27) Tchitchevka, D. S.; Ponrouch, A.; Verrelli, R.; Broux, T.; Frontera, C.; Sorrentino, A.; Bardé, F.; Biskup, N.; Arroyo-de Dompablo, M. E.; Palacín, M. R. Electrochemical Intercalation of Calcium and Magnesium in TiS<sub>2</sub>: Fundamental Studies Related to Multivalent Battery Applications. *Chem. Mater.* **2018**, *30*, 847–856.
- (28) Emly, A.; Van der Ven, A. Mg Intercalation in Layered and Spinel Host Crystal Structures for Mg Batteries. *Inorg. Chem.* **2015**, *54*, 4394–4402.
- (29) Kolli, S. K.; Van der Ven, A. Controlling the Electrochemical Properties of Spinel Intercalation Compounds. *ACS Applied Energy Materials* **2018**, *1*, 6833–6839.
- (30) Ling, C.; Suto, K. Thermodynamic Origin of Irreversible Magnesium Trapping in Chevrel Phase Mo<sub>6</sub>S<sub>8</sub>: Importance of Magnesium and Vacancy Ordering. *Chem. Mater.* **2017**, *29*, 3731–3739.
- (31) Rong, Z.; Malik, R.; Canepa, P.; Sai Gautam, G.; Liu, M.; Jain, A.; Persson, K.; Ceder, G. Materials Design Rules for Multivalent Ion Mobility in Intercalation Structures. *Chem. Mater.* **2015**, *27*, 6016–6021.
- (32) Lacivita, V.; Wang, Y.; Bo, S.-H.; Ceder, G. Ab initio investigation of the stability of electrolyte/electrode interfaces in all-solid-state Na batteries. *J. Mater. Chem. A* **2019**, *7*, 8144–8155.
- (33) Tang, H.; Deng, Z.; Lin, Z.; Wang, Z.; Chu, I.-H.; Chen, C.; Zhu, Z.; Zheng, C.; Ong, S. P. Probing Solid-Solid Interfacial Reactions in All-Solid-State Sodium-Ion Batteries with First-Principles Calculations. *Chem. Mater.* **2018**, *30*, 163–173.
- (34) Zhu, Y.; He, X.; Mo, Y. Origin of Outstanding Stability in the Lithium Solid Electrolyte Materials: Insights from Thermodynamic Analyses Based on First-Principles Calculations. *ACS Appl. Mater. Interfaces* **2015**, *7*, 23685–23693.
- (35) Culver, S. P.; Koerver, R.; Zeier, W. G.; Janek, J. On the Functionality of Coatings for Cathode Active Materials in Thiophosphate-Based All-Solid-State Batteries. *Adv. Energy Mater.* **2019**, *9*, 1900626.
- (36) Van der Ven, A.; Ceder, G.; Asta, M.; Tepesch, P. D. First-principles theory of ionic diffusion with nondilute carriers. *Phys. Rev. B: Condens. Matter Mater. Phys.* **2001**, *64*, 184307.
- (37) Sai Gautam, G.; Canepa, P.; Urban, A.; Bo, S.-H.; Ceder, G. Influence of inversion on Mg mobility and electrochemistry in spinels. *Chem. Mater.* **2017**, *29*, 7918–7930.
- (38) Sun, X.; Bonnick, P.; Duffort, V.; Liu, M.; Rong, Z.; Persson, K. A.; Ceder, G.; Nazar, L. F. A high capacity thiospinel cathode for Mg batteries. *Energy Environ. Sci.* **2016**, *9*, 2273–2277.
- (39) Ahmed, S.; et al. Enabling fast charging – A battery technology gap assessment. *J. Power Sources* **2017**, *367*, 250–262.
- (40) Ohta, N.; Takada, K.; Sakaguchi, I.; Zhang, L.; Ma, R.; Fukuda, K.; Osada, M.; Sasaki, T. LiNbO<sub>3</sub>-coated LiCoO<sub>2</sub> as cathode material

- for all solid-state lithium secondary batteries. *Electrochim. Commun.* **2007**, *9*, 1486–1490.
- (41) Henkelman, G.; Jónsson, H. Improved tangent estimate in the nudged elastic band method for finding minimum energy paths and saddle points. *J. Chem. Phys.* **2000**, *113*, 9978–9985.
- (42) Sheppard, D.; Terrell, R.; Henkelman, G. Optimization methods for finding minimum energy paths. *J. Chem. Phys.* **2008**, *128*, 134106.
- (43) Hohenberg, P.; Kohn, W. Inhomogeneous Electron Gas. *Phys. Rev.* **1964**, *136*, B864–B871.
- (44) Kohn, W.; Sham, L. J. Self-Consistent Equations Including Exchange and Correlation Effects. *Phys. Rev.* **1965**, *140*, A1133–A1138.
- (45) Kresse, G.; Hafner, J. Ab initiomolecular dynamics for liquid metals. *Phys. Rev. B: Condens. Matter Mater. Phys.* **1993**, *47*, 558–561.
- (46) Kresse, G.; Furthmüller, J. Efficient iterative schemes for ab initio total-energy calculations using a plane-wave basis set. *Phys. Rev. B: Condens. Matter Mater. Phys.* **1996**, *54*, 11169–11186.
- (47) Perdew, J. P.; Burke, K.; Ernzerhof, M. Generalized Gradient Approximation Made Simple. *Phys. Rev. Lett.* **1996**, *77*, 3865–3868.
- (48) Kresse, G.; Joubert, D. From ultrasoft pseudopotentials to the projector augmented-wave method. *Phys. Rev. B: Condens. Matter Mater. Phys.* **1999**, *59*, 1758–1775.
- (49) Jain, A.; Ong, S. P.; Hautier, G.; Chen, W.; Richards, W. D.; Dacek, S.; Cholia, S.; Gunter, D.; Skinner, D.; Ceder, G.; Persson, K. A. Commentary: The Materials Project: A materials genome approach to accelerating materials innovation. *APL Mater.* **2013**, *1*, No. 011002.
- (50) Heyd, J.; Scuseria, G. E.; Ernzerhof, M. Hybrid functionals based on a screened Coulomb potential. *J. Chem. Phys.* **2003**, *118*, 8207–8215.
- (51) Heyd, J.; Scuseria, G. E.; Ernzerhof, M. Erratum: “Hybrid functionals based on a screened Coulomb potential” [J. Chem. Phys. 118, 8207 (2003)]. *J. Chem. Phys.* **2006**, *124*, 219906.
- (52) Krakau, A. V.; Vydróv, O. A.; Izmaylov, A. F.; Scuseria, G. E. Influence of the exchange screening parameter on the performance of screened hybrid functionals. *J. Chem. Phys.* **2006**, *125*, 224106.
- (53) Jain, A.; Hautier, G.; Moore, C. J.; Ong, S. P.; Fischer, C. C.; Mueller, T.; Persson, K. A.; Ceder, G. A high-throughput infrastructure for density functional theory calculations. *Comput. Mater. Sci.* **2011**, *50*, 2295–2310.
- (54) Au-Yang, M. Y.; Cohen, M. L. Electronic Structure and Optical Properties of Mg<sub>2</sub>Si, Mg<sub>2</sub>Ge, and Mg<sub>2</sub>Sn. *Phys. Rev.* **1969**, *178*, 1358–1364.
- (55) Meutzner, F.; Nestler, T.; Zschornak, M.; Canepa, P.; Gautam, G. S.; Leoni, S.; Adams, S.; Leisegang, T.; Blatov, V. A.; Meyer, D. C. Computational analysis and identification of battery materials. *Physical Sciences Reviews* **2019**, *4*, 20180044.
- (56) Wang, Y.; Richards, W. D.; Ong, S. P.; Miara, L. J.; Kim, J. C.; Mo, Y.; Ceder, G. Design principles for solid-state lithium superionic conductors. *Nat. Mater.* **2015**, *14*, 1026–1031.
- (57) He, X.; Zhu, Y.; Mo, Y. Origin of fast ion diffusion in superionic conductors. *Nat. Commun.* **2017**, *8*, 15893.
- (58) Liu, M.; Rong, Z.; Malik, R.; Canepa, P.; Jain, A.; Ceder, G.; Persson, K. A. Spinel compounds as multivalent battery cathodes: a systematic evaluation based on ab initio calculations. *Energy Environ. Sci.* **2015**, *8*, 964–974.
- (59) Freysoldt, C.; Neugebauer, J.; Van de Walle, C. G. Fully *Ab Initio* Finite-Size Corrections for Charged-Defect Supercell Calculations. *Phys. Rev. Lett.* **2009**, *102*, 016402.
- (60) Kumagai, Y.; Oba, F. Electrostatics-based finite-size corrections for first-principles point defect calculations. *Phys. Rev. B: Condens. Matter Mater. Phys.* **2014**, *89*, 195205.
- (61) Kröger, F.; Vink, H. Relations between the Concentrations of Imperfections in Crystalline Solids. *Solid State Phys.* **1956**, *3*, 307–435.
- (62) Chen, T.; Sai Gautam, G.; Huang, W.; Ceder, G. First-Principles Study of the Voltage Profile and Mobility of Mg Intercalation in a Chromium Oxide Spinel. *Chem. Mater.* **2018**, *30*, 153–162.
- (63) Gautam, G. S.; Canepa, P.; Malik, R.; Liu, M.; Persson, K.; Ceder, G. First-principles evaluation of multi-valent cation insertion into orthorhombic V<sub>2</sub>O<sub>5</sub>. *Chem. Commun.* **2015**, *51*, 13619–13622.
- (64) Yoo, H. D.; Jokisaari, J. R.; Yu, Y.-S.; Kwon, B. J.; Hu, L.; Kim, S.; Han, S.-D.; Lopez, M.; Lapidus, S. H.; Nolis, G. M. Intercalation of Magnesium into a Layered Vanadium Oxide with High Capacity. *ACS Energy Letters* **2019**, *4*, 1528–1534.
- (65) Hannah, D. C.; Sai Gautam, G.; Canepa, P.; Ceder, G. On the Balance of Intercalation and Conversion Reactions in Battery Cathodes. *Adv. Energy Mater.* **2018**, *8*, 1800379.
- (66) Kim, C.; Phillips, P. J.; Key, B.; Yi, T.; Nordlund, D.; Yu, Y.-S.; Bayliss, R. D.; Han, S.-D.; He, M.; Zhang, Z.; Burrell, A. K.; Klie, R. F.; Cabana, J. Direct Observation of Reversible Magnesium Ion Intercalation into a Spinel Oxide Host. *Adv. Mater.* **2015**, *27*, 3377–3384.
- (67) Sai Gautam, G.; Canepa, P.; Abdellahi, A.; Urban, A.; Malik, R.; Ceder, G. The Intercalation Phase Diagram of Mg in V<sub>2</sub>O<sub>5</sub> from First-Principles. *Chem. Mater.* **2015**, *27*, 3733–3742.
- (68) Van der Ven, A.; Ceder, G. Lithium Diffusion in Layered Li<sub>x</sub>CoO<sub>2</sub>. *Electrochim. Solid-State Lett.* **1999**, *3*, 301.
- (69) Gautam, G. S.; Sun, X.; Duffort, V.; Nazar, L. F.; Ceder, G. Impact of intermediate sites on bulk diffusion barriers: Mg intercalation in Mg<sub>2</sub>Mo<sub>3</sub>O<sub>8</sub>. *J. Mater. Chem. A* **2016**, *4*, 17643–17648.
- (70) Van der Ven, A.; Thomas, J. C.; Xu, Q.; Swoboda, B.; Morgan, D. Nondilute diffusion from first principles: Li diffusion in Li<sub>x</sub>TiS<sub>2</sub>. *Phys. Rev. B: Condens. Matter Mater. Phys.* **2008**, *78*, 104306.
- (71) Lei, Y.; Gong, Y.; Duan, Z.; Wang, G. Density functional calculation of activation energies for lattice and grain boundary diffusion in alumina. *Phys. Rev. B: Condens. Matter Mater. Phys.* **2013**, *87*, 214105.
- (72) Dylla, A. G.; Xiao, P.; Henkelman, G.; Stevenson, K. J. Morphological Dependence of Lithium Insertion in Nanocrystalline TiO<sub>2</sub>(B) Nanoparticles and Nanosheets. *J. Phys. Chem. Lett.* **2012**, *3*, 2015–2019.
- (73) Sun, W.; Bartel, C. J.; Arca, E.; Bauers, S. R.; Mathews, B.; Orvañanos, B.; Chen, B.-R.; Toney, M. F.; Schelhas, L. T.; Tumas, W.; Tate, J.; Zakutayev, A.; Lany, S.; Holder, A. M.; Ceder, G. A map of the inorganic ternary metal nitrides. *Nat. Mater.* **2019**, *18*, 732–739.
- (74) Lee, J.; Urban, A.; Li, X.; Su, D.; Hautier, G.; Ceder, G. Unlocking the Potential of Cation-Disordered Oxides for Rechargeable Lithium Batteries. *Science* **2014**, *343*, 519–522.
- (75) Butler, K. T.; Sai Gautam, G.; Canepa, P. Designing interfaces in energy materials applications with first-principles calculations. *npj Computational Materials* **2019**, *5*, 19.